frontiers | Frontiers in Earth Science

BRIEF RESEARCH REPORT
published: 28 April 2022
doi: 10.3389/feart.2022.838532

Pumice Raft Detection Using Machine-Learning on Multispectral Satellite Imagery

Maggie Zheng[1], Tushar Mittal[1]*, Kristen E. Fauria[2], Ajit Subramaniam[3] and Martin Jutzeler[4]*

[1]Department of Earth, Atmospheric and Planetary Sciences, Massachusetts Institute of Technology, Cambridge, MA, United States, [2]Department of Earth and Environmental Sciences, Vanderbilt University, Nashville, TN, United States, [3]Lamont-Doherty Earth Observatory, Columbia University, Palisades, NY, United States, [4]Centre for Ore Deposit and Earth Sciences (CODES), University of Tasmania, Hobart, TAS, Australia

Most of Earth's volcanic eruptions occur underwater, and these submarine eruptions can significantly impact large-scale Earth systems (e.g., enhancing local primary production by phytoplankton). However, detecting submarine eruptions is challenging due to their remote locations, short eruption durations, lack of sea surface signature (if eruptions do not breach the surface), and the transient nature of the surface manifestations of an eruption (e.g., floating pumice clasts, hydrothermal fluids). We can utilize global satellite imagery of 10–30 m resolution (e.g., Landsat 8, Sentinel-2) to detect new eruptions; however, the large data volumes make it challenging to systematically analyze satellite imagery globally. In this study, we address these challenges by developing a new semi-automated analysis framework to detect submarine eruptions through supervised classification of satellite images on Google Earth Engine. We train our algorithm using images from rafts produced by the August 2019 eruption of Volcano F in the Tofua Arc and present a case study using our methodology on satellite imagery from the Rabaul caldera region in Papua New Guinea. We potentially find a large number of new unreported pumice rafts (in ~16% of images from 2017–present). After analysis of the spatial pattern of raft sightings and ancillary geophysical and visual observations, we interpret that these rafts are not the result of a new eruption. Instead, we posit that the observed rafts represent remobilization of pumice clasts from previous historical eruptions. This novel process of raft remobilization may be common at near-shore/partially submarine caldera systems (e.g., Rabaul, Krakatau) and may have significant implications for new submarine eruption detection and volcanic stratigraphy.

Keywords: submarine volcano monitoring, pumice raft dispersal, machine learning (ML), sentinel-2, Google Earth engine (GEE)

OPEN ACCESS

Edited by:
Max Rudolph,
University of California, Davis, United States

Reviewed by:
Simon Carn,
Michigan Technological University, United States
Scott Edward Bryan,
Queensland University of Technology, Australia

****Correspondence:***
Maggie Zheng
mzhengxi@mit.edu
Tushar Mittal
tmittal2@mit.edu

Specialty section:
This article was submitted to Volcanology, a section of the journal Frontiers in Earth Science

Received: *17 December 2021*
Accepted: *04 April 2022*
Published: *28 April 2022*

Citation:
Zheng M, Mittal T, Fauria KE, Subramaniam A and Jutzeler M (2022) Pumice Raft Detection Using Machine-Learning on Multispectral Satellite Imagery. Front. Earth Sci. 10:838532. doi: 10.3389/feart.2022.838532

1 INTRODUCTION

Submarine volcanism is an important driver for Earth's climate and geochemical cycles on global scales (mid-ocean ridge volcanic system and submarine large igneous provinces) as well as on regional scales (Embley et al., 2004; Santana-Casiano et al., 2013; Tilstone et al., 2014; Kelley, 2017; Mittal and Delbridge, 2019). For instance, submarine eruptions inject ash, pumice, and magmatic volatiles (with nutrients such as Fe) into the water column and the atmosphere (White et al., 2015). Pumice rafts, one of the key signatures of some submarine eruptions, can transport volcanic products

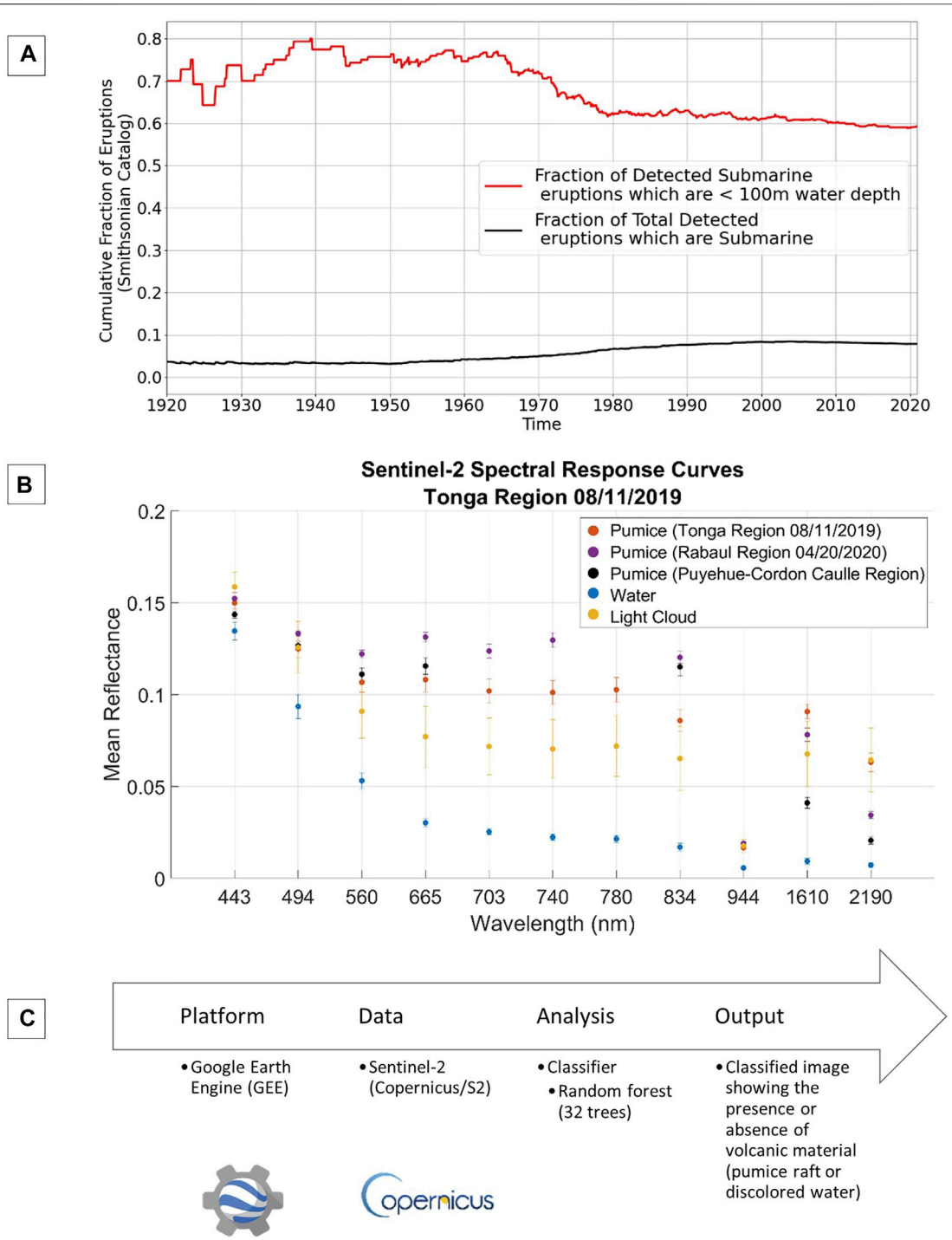

FIGURE 1 | (A) Fraction of all detected submarine eruptions out of total eruptions and fraction of detected shallow submarine eruptions (less than 100 m water depth) out of all detected submarine eruptions (Global Volcanism Program, 2013). Only a small fraction of submarine eruptions are pumice-forming. **(B)** Mean spectral response curves generated for a Sentinel-2 raft image in the Tonga region (11 August 2019). Error bars are generated from the standard deviation measured for each wavelength. Spectral response curves for pumice from the Rabaul region (20 April 2020) and a lake near Puyehue-Cordón Caulle are also provided for comparison. For Puyehue-Cordón Caulle, Sentinel-2 imagery was not available, so Landsat 8 imagery was used instead, and mean reflectance values were averaged between two dates (19 June 2013 and 5 October 2013). **(C)** Schematic of workflow used in this study.

and marine organisms across thousands of kilometers, potentially dispersing nutrients and increasing microbial biomass and biodiversity in areas geographically distant from the site of the eruption (DeVantier, 1992; Risso et al., 2002; Bryan et al., 2012). Pumice rafts can also be a significant hazard for human maritime activities, especially by clogging harbors and affecting near shore sea life and fisheries, disrupting local economies (Bryan et al., 2012; Jutzeler et al., 2020), as observed in the recent raft dispersal from the 2021 eruption of Fukutoku-Okanoba volcano, a submarine volcano in the Bonin Arc (24.285° N, 141.481° E) (Fauria et al., 2022; Yoshida et al., 2022).

Modern day submarine volcanism includes both mid-ocean ridge and ocean-island volcanism as well as fully/partially submarine subduction zone volcanism (e.g., Kermadec-Tonga Arc, Izu-Bonin Arc, Papua New Guinea Arc) (White et al., 2006; Global Volcanism Program, 2013). Overall, submarine volcanism potentially represents the majority (> 70%) of Earth's present-day volcanism (White et al., 2006; White et al., 2015; ERUPT, 2017; Rubin et al., 2012). However, we have historically detected only a very small fraction of expected underwater eruptions. In fact, only ~10% of all eruptions in the Smithsonian Global Volcanism database (Global Volcanism Program, 2013) over the past 100 years are submarine (**Figure 1A**, (White et al., 2006)) and the majority of detected eruptions are shallow (< 100 m water depth; **Figure 1A**).

One of the key reasons for this strong bias in our submarine eruption detection ability is the remote location of submarine volcanoes, as well as the difficulty in detecting eruptions that may or may not breach the sea surface. In addition, unlike subaerial volcanoes, precursory gas emissions or thermal anomalies are much more difficult to detect beneath the water surface. Although multiple new approaches have been proposed to improve submarine volcanism detection, including hydro-acoustics [e.g., (Heaney et al., 2013; Tepp et al., 2019)], seismic and ground deformation with ocean bottom seismometers (Wilcock et al., 2016; Matsumoto et al., 2019; Cesca et al., 2020; Tepp and Dziak, 2021), and ocean thermal anomalies (Baker et al., 1989; Mittal and Delbridge, 2019), challenges remain due to limited global instrumental coverage. In this study, we describe another dataset—satellite imagery—that can be used to efficiently detect and characterize products of submarine volcanism.

Automated satellite image analysis has already proven to be very useful for global subaerial eruption detections based on thermal anomalies, ash-rich subaerial plumes, and sulfur dioxide emissions (Wright et al., 2004; Brenot et al., 2014; Furtney et al., 2018; Poland et al., 2020; Engwell et al., 2021). However these methods are not adapted for submarine eruptions where the presence of water obscures/reduces these signatures. Satellite imagery has been used to map the eruptive products (e.g., pumice, ash, hydrothermal fluids) from submarine eruptions (Bryan et al., 2004; Jutzeler et al., 2014; O'Malley et al., 2014; Jutzeler et al., 2020; Sakuno, 2021; Whiteside et al., 2021) on an event-by-event basis. For example, a pumice raft from the 7 August 2019 Tonga eruption of an unnamed submarine volcano (sometimes referred to as Volcano F, 18.325°S, 174.365°W) in the Tofua Arc was tracked in near-real-time by Sentinel-2 (~10 m/pixel) and Landsat 8 (~30 m/pixel) satellite imagery (Jutzeler et al., 2020). However, this was done by manual hand-tracing and visual tracking through various satellite images. Although this process is fairly accurate for large rafts, it introduces subjectivity in tracing, especially for smaller rafts. Consequently, it is difficult to quantify uncertainties and biases across different studies. An ancillary challenge with using satellite imagery is the large data volume associated with satellite collections. For example, a single day in the Tonga region is composed of about forty individual 100 × 100 km image granules, each containing about 600 MB of data. Thus, analyzing entire global collections over extended time periods, and for multiple different satellites, would require handling enormous amounts of data and requisite computing resources.

Our study aims to address these challenges of submarine eruption detection by developing a semi-automated Machine-Learning (ML) based methodology using global, publicly available, high resolution (~ <30 m/pixel) satellite data products (**Figure 1C**). This method utilizes Google Earth Engine (Gorelick et al., 2017), in order to remove the large data storage need that is typical for analyzing satellite collections. Our primary focus is on detecting rafts formed from floating pumice (or pumiceous material, **Supplementary Text S16**) emitted by intermediate to silicic volcanism, but our approach can be applied to other signatures of submarine eruptions (e.g., discolored water from hydrothermal fluids). Our analysis is complementary to recent work on detection of large submarine eruptions using specific global, low resolution (> 250 m/pixel) satellite products (O'Malley et al., 2014; Qi et al., 2020; Whiteside et al., 2021).

As a complementary question, we also seek to examine whether individual pumice raft detections necessarily indicate a new eruption. Previous work has examined the remobilization of pumice clasts, which may have been deposited in the area immediately surrounding the vent, or stranded a distance away after traveling as a raft, following large eruptions (Mandeville et al., 1996; Shane et al., 1998; Manville et al., 2002; Jutzeler et al., 2020). Using our automated detection algorithms, we can improve raft detection (of scales of at least a few pixel scale, e.g., a few 100 m^2 for Sentinel-2 imagery and even smaller with commercial sub-m pixel scale imagery). These observational constraints on pumice raft occurrence, along with field studies of the detected rafts and textural analysis, can help understand the re-rafting mobility and floatation ability of pumice of different sizes on timescales ranging from days to hundreds of years after the original eruption (Brasier et al., 2011; Bryan et al., 2012).

In **Section 2**, we describe our detection algorithm and its implementation in Google Earth Engine. In **Section 3**, we illustrate our method's accuracy using satellite imagery from the 2019 Tonga submarine eruption (Jutzeler et al., 2020) and then use our method to analyze pumice rafts in a region close to the Rabaul volcano in Papua New Guinea (partially submerged caldera). In **Section 4**, we discuss what our new pumice raft detections from Rabaul suggest in regards to suspension of pumice material, potentially from pumice clasts or rafts previously washed up on shores or eroded on riverbanks or coastal cliffs. Finally, we briefly discuss areas for future algorithmic improvements.

2 MATERIALS AND METHODS

2.1 Google Earth Engine

We developed and implemented our Machine Learning (ML) detection algorithm for pumice raft detection on the Google Earth Engine (GEE) platform (Gorelick et al., 2017). GEE is a web-based, publicly available platform that enables access to a vast catalog of satellite images and the resources to run global-scale analyses without the need to download or export large amounts of data. There are various satellite collections offered through GEE, such as low resolution (MODIS) and medium-high resolution imagery (Landsat, Sentinel-2). Although some other super-high-resolution image collections are available outside of GEE (e.g., Planet labs—3 m/pixel, Digital Globe—50 cm/pixel), they are typically not publicly available without commercial licenses. Thus, for this study, we have primarily focused on using GEE resources for the ML algorithm.

Specifically, we use GEE collections from the Sentinel-2 Multi-Spectral Instrument (MSI) as our baseline satellite product. Sentinel-2 (a pair of two satellites, each with MSI instrumentation) offers both high-resolution imagery (10–60 m/pixel), good coverage in regions of interest, and a relatively frequent repeat time (~global 5-day revisits; **Supplementary Text S6**). Sentinel-2 data products are also freely available through the European Space Agency's Copernicus Open Access Hub as well as other cloud environments. For our study, we chose to use Sentinel-2 as its high resolution imagery could be used to detect much smaller rafts than a lower resolution satellite (e.g., MODIS). In addition, Sentinel-2's MSI collects data across 13 different spectral bands, with finer spectral coverage than other high resolution satellite image collections (e.g., Landsat 7 and 8) (See spectral response curve for Landsat 8 image of Puyehue-Cordón Caulle pumice in **Figure 1B**). An initial method using thresholds on only the visual bands to detect pumice rafts was insufficient, so the additional spectral bands are necessary in our ML algorithm (**Supplementary Text S1**). As illustrated by the variable importance in the Random Forest classifier (RF, **Supplementary Figure S11**), the multi-wavelength information is critical for accurate classification with a dominant role of the visible bands. In particular, the reflectance of pumice in the near-infrared (NIR) bands (700–900 nm) is much higher than the reflectance at those bands of most biological phenomena that are near the surface but still underwater (i.e., algal blooms, coral spawn, seaweed) (Biermann et al., 2020; Qi et al., 2020), so the NIR bands are critical for distinguishing between pumice and other visually similar-looking biological blooms. Our overall methodology is general and can be applied to other satellite collections in the future (**Supplementary Text S10**).

2.2 Machine-Learning Algorithm

To identify spectral characteristics that can be used to classify Sentinel-2 image pixels as pumice rafts, we generated spectral response curves for pumice and other categories of interest in **Figure 1B**. Spectral response curves record the mean reflectance or brightness of an image pixel for a range of wavelengths. We used the Tonga pumice raft from 11 August 2019 to generate the spectral response curves (**Figure 1B**), as the particular eruption and the associated raft has been extensively analyzed by previous work (Brandl et al., 2020; Jutzeler et al., 2020). We also show the variance around the mean spectral response curve calculated for all of the pixels for each class (pumice, water, light clouds).

A key result from this analysis is that there is a significant difference between the spectral response curves of pumice, water, and light clouds (**Figure 1B**). Additionally, we find relatively minor (compared to differences with other classes) variation in the reflectance from pumice pixels within a single geo-temporal area, such as a specific day in Tonga (**Figure 1B**) or comparing across multiple days for the same raft (**Supplementary Figure S16**). Although there is some variation in pumice spectral response curves when comparing rafts from different chemical compositions, sources, and times (**Figure 1B**, comparison with Rabaul raft and Puyehue-Cordón Caulle raft), the general shape of the reflectance curve remains very similar. This characteristic shape of the spectral response curve for pumice pixels allows for an algorithm to identify pumice and differentiate from other classes (e.g., water, clouds) across a broad range of regions and time periods. Details for the Puyehue-Cordón Caulle raft are provided in **Supplementary Text S13**.

Our machine-learning algorithm uses a Random Forest classifier to read in an RGB Sentinel-2 image and return a classified image, where each pixel is colored according to the assigned class. The algorithm specifics are detailed in **Supplementary Text S4**. Since RF is a supervised learning algorithm, we need to train it on a set of manually demarcated and classified pixels. Our primary training data for pumice, ocean water, light cloud cover, and heavy cloud cover was sampled from the Tonga raft on 11 August 2019 (**Figure 2A**, only a small part of the raft pixels were used for training). We also included additional data from a Sentinel-2 scene of Rabaul, Papua New Guinea, on 20 April 2020 (**Figure 2B**, spectrally this is representative of the potential rafts from other days also). This image includes a large, distinct pumice raft as well as ocean water, light cloud cover, pumice mixture classes, and two different discolored water classes (additional information for the discolored water classes are included in **Supplementary Text S9**). Since the discolored water classes are not the primary focus of this study, our primary optimization for the RF algorithm was to ensure accurate detection of pumice rafts. We provide all the scripts, with step-by-step instructions for usage, used in our analysis in a publicly available repository (**Supplementary Material**—GEE Script Links).

3 RESULTS

3.1 Single Image Analysis Results

We applied our classification algorithm to Sentinel-2 images from different geo-temporal regions to test model accuracy (**Figure 2**). In the Tonga area on 11 August 2019 (**Figure 2A**), the classifier displays pumice pixels in red, water in blue, light cloud cover in orange, and heavy cloud cover in white. The shape of the large raft is distinctly visible in the classified image. In the Rabaul region, on

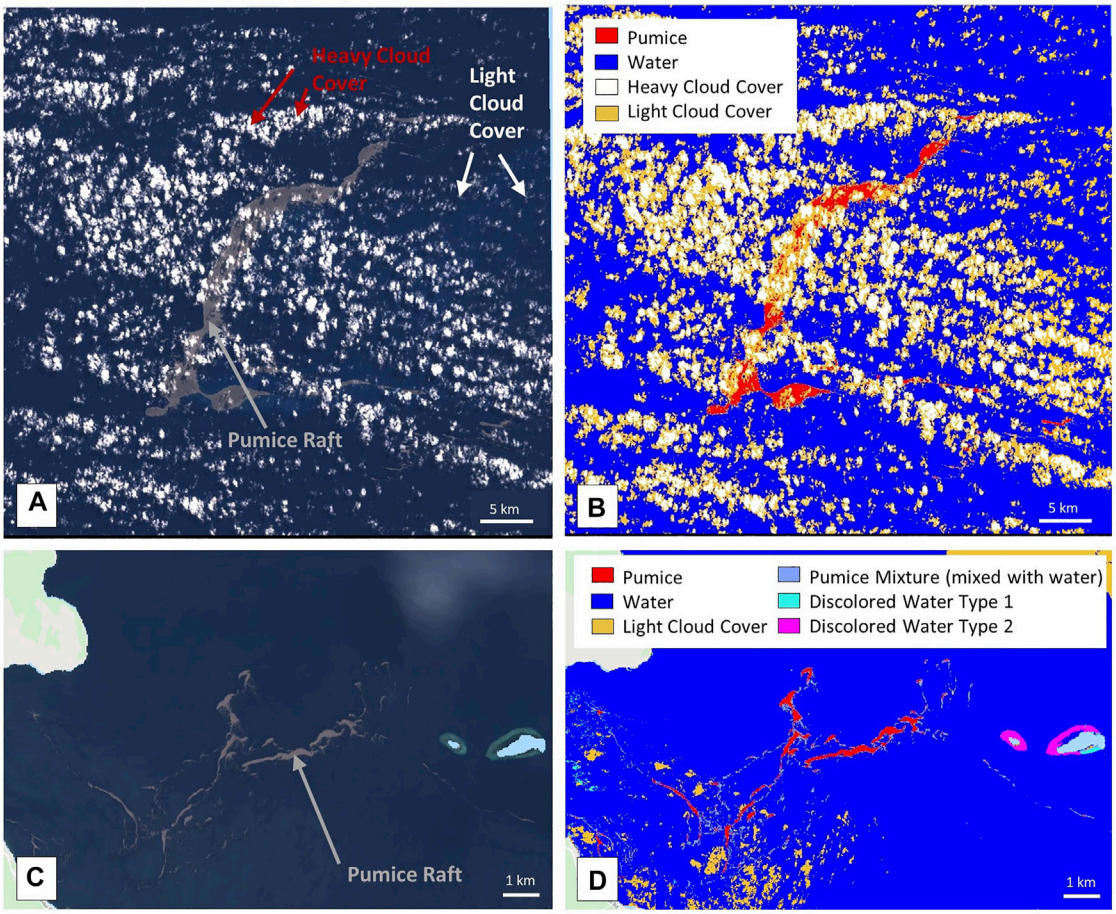

FIGURE 2 | (A) Land-masked RGB image of Tonga region on 08/11/2019 **(B)** Classified image of Tonga region on 08/11/2019 **(C)** Land-masked RGB image of Rabaul on 04/20/2020 **(D)** Land-masked classified image of Rabaul on 04/20/2020.

20 April 2020 (**Figure 2A**), the classifier also includes additional classes: mixed/faint pumice—a mixture of water and pumice—shown in light blue, and two different classes of discolored water shown in turquoise and magenta. Overall, our algorithm is efficient at identifying pumice from other backgrounds though the accuracy of discolored water detection (mixing with corals) and shallow cloud is not great at present. Algorithm validation methods and results are included in **Supplementary Text S5**.

3.2 Regional Results

To assess the utility of our algorithm for new submarine eruption detection, we applied the classifier over a single region for an extended period of time. We focused on Rabaul, a partially submarine volcano located on the Gazelle Peninsula's tip at the northeast end of New Britain in Papua New Guinea (**Figure 3A**). The Rabaul caldera (~8 × 14 km size) was formed as a consequence of multiple large explosive eruptions in the past few hundred thousand years, with the present day shape due to an eruption ~1,400 years ago (GVP and wunderman, 1994). The caldera is mostly shallow submarine (< 200 m water depth) and is connected to the sea on the east through a wide opening (Blanche Bay). The main raft-forming eruptions for this volcano occurred in 1878, 1937, and 1994, and no raft formation has been recorded since 1994 (GVP and Wunderman, 1994; GVP and Wunderman, 2006). No activity has been recorded at either of the main vents (Vulcan and Tavurvur) since 2014 (Bernard and Bouvet de Maisonneuve, 2020). More detailed eruption history is provided in **Supplementary Text S8**.

In the Rabaul area, we applied our algorithm from November 2015 (start of the Sentinel-2 coverage for the Rabaul region) to August 2020—a total of 239 distinct days with images. More details on our algorithm application method are included in **Supplementary Text S7**.

Of these 239 days, we found that 74 days were too cloudy for the classifier to detect any pumice meaningfully. Cloudy days were filtered out by manually examining classified images and removing images in which every pixel was labeled as heavy or light cloud cover. In the future, this step can be automated by explicitly filtering the images based on the classified heavy cloud fraction. We detected potential rafts in 28 (red lines, **Figure 3B**)

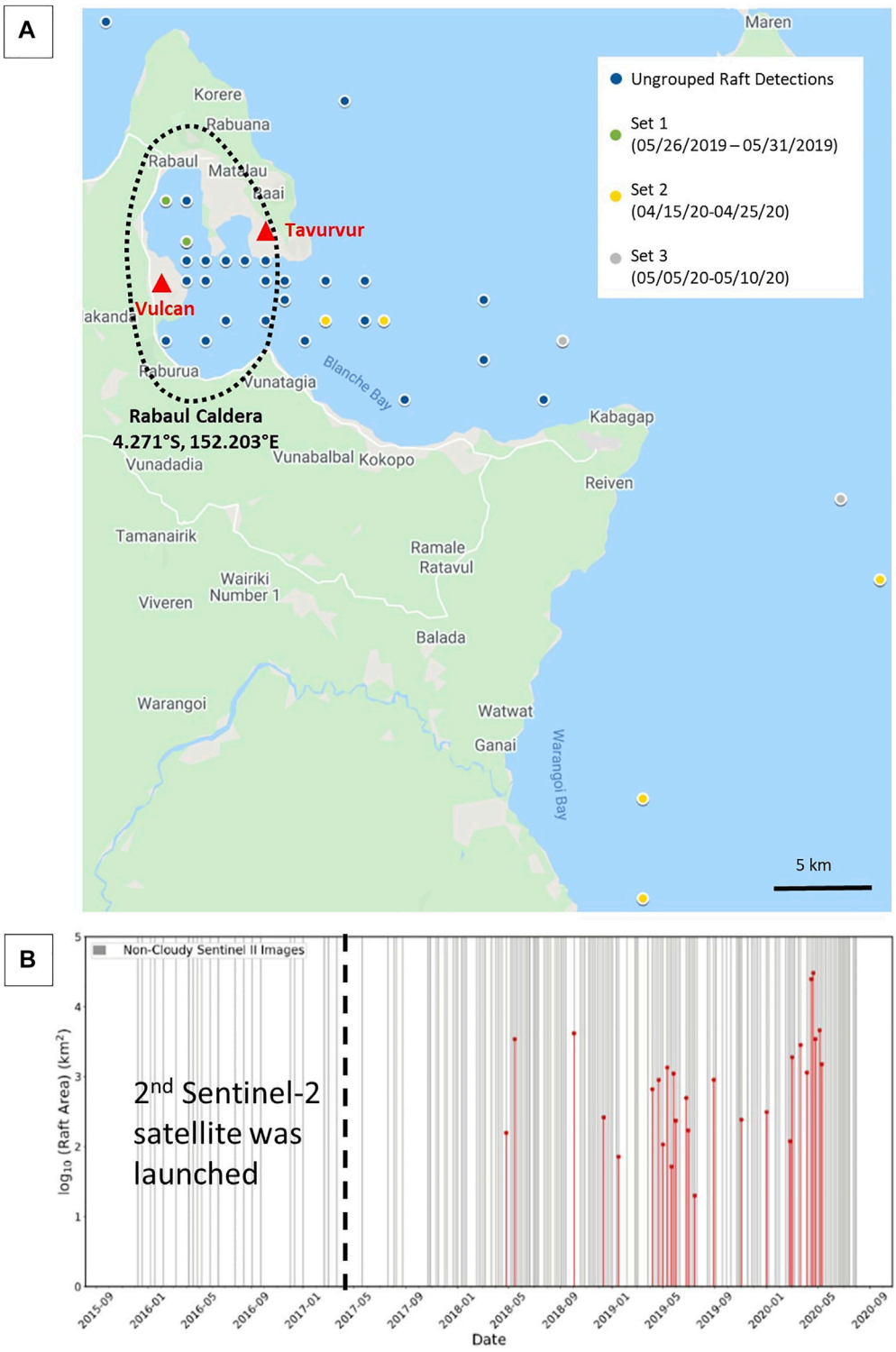

FIGURE 3 | (A) Map of pumice raft detection locations in Rabaul area. Main vent locations are marked with red triangles. Groupings of raft detections (by proximity in time and location) are indicated by the different colored icons **(B)** Non-cloudy days during Sentinel-2 coverage period, with raft detections in red (height indicating raft area).

of the remaining 165 days (gray lines, **Figure 3B**), leading to a detection rate of 16.97%. As illustrated in **Figure 3B**, most of our raft detections were after January 2018 (**Figure 3B**). This is likely a consequence of increased revisit frequency (~5-day) after the second Sentinel-2 satellite launch. Before 2018, when only one Sentinel-2 satellite was in operation, there are significantly fewer images available. It is noteworthy that none of the rafts detected in our analysis had been previously reported in the scientific literature (to the best of our knowledge) or the Smithsonian Global Volcanism Catalog (Global Volcanism Program, 2013). The sizes of our detected rafts varied greatly, with raft areas as small as 20 km^2 to as great as 10,000 km^2. At present, we do not have any direct ground truthing of our detections. However, considering the distinctive spectral features of pumice compared to other biological sources, especially in the Near Infrared (Biermann et al., 2020; Qi et al., 2020), we interpret the classified features as rafts of pumiceous material - pumice rafts (**Supplementary Text S16** for discussion regarding difference between "true" pumice and more general pumiceous material).

3.2.1 Source of New Rafts in Rabaul

Given our new raft detections, there is a natural follow-up question—do these rafts represent previously unreported submarine eruptions, or are they suspended pumiceous material remobilized from known previous eruption deposits from Rabaul or pumice produced by eruptions from other volcanoes in the region that subsequently drifted into the Rabaul harbor? These are the three primary end-member models, with the remobilization of pumice (or pumiceous material) from previous eruptions being a process that has been documented following the dispersal of large pumice rafts. For example, the Tonga 2019 pumice raft was stranded in near coastal regions in multiple islands in Fiji (in particular Lakeba island) in early-mid September 2019. However, some of this raft material in Lakeba island was not remobilized till late October-early November 2019 (Jutzeler et al., 2020, observations from Sentinel-2 Imagery). Redeposition and remobilization of volcanic products such as ash fall (Etyemezian et al., 2019; Del Bello et al., 2021) as well as subaerial [e.g., from Pinatubo 1991 eruption, Torres et al. (1996)] and subaqueous pyroclastic material has been recorded after initial deposition (Mandeville et al., 1996; Manville et al., 2002; Park and Schmincke, 2020). However, the majority of this work has focused on a short time frame—on the order of days to months after the eruption though there are some exceptions—e.g., secondary pumice rafts from Socorro Island in January 2009 (Ochoa, 2009, Personal Comm. from Scott Bryan) and secondary pumice rafts in Brasier et al. (2011). Here, if our hypothesis is correct, the pumiceous material we are seeing is remobilized tens or even hundreds of years after the original eruption since the last major raft forming eruption in Rabaul was in 1994.

We assess the likelihood of new submarine eruptions by analyzing the reported volcanic activity for Rabaul in the Smithsonian Volcano Catalog (Global Volcanism Program, 2013). The Rabaul Volcano Observatory has recorded no large eruptions since 2014 (Global Volcanism Program, 2013) and/or any significant submarine activity besides hydrothermal discharge near the Tavurvur vent. Because rafts initiating from point sources can indicate new eruptions, we test this further by recording each of our raft detections' spatial location and considering the spread of each sighting. We have tried to manually aggregate three sets of raft locations together (**Figure 3A**). These sets are of sequential images, in which the raft detections were somewhat close, not only in time, but in location as well. Conclusively tracking the rafts as they are advected around by local ocean currents is challenging due to repeat frequency (5-day gap between images), cloud cover, and complex shallow-water ocean currents in the regions. In aggregate, the detections are scattered over a broad area in the caldera and surrounding sea, rather than primarily located near any known vents (**Figure 3A**).

We also used Sentinel-2 imagery as well as ancillary datasets [e.g., higher spatial and temporal resolution Planet Labs imagery (Planet Team, 2021)] to check if the rafts are associated with any other eruptive signatures expected for shallow submarine eruptions (e.g., aerial plumes, discolored water). We did not find any aerial plumes and, while there was some discolored water around the Tavurvur vent location, we did not find any relationship between the days with raft detections and days with discolored water around the vent (**Supplementary Text S14**). Thus, we interpret that the detected rafts are not actually products from a new submarine eruption.

Instead, we propose that they are secondary rafts [like the rafts in Socorro Island in January 2009 (Ochoa (2009), Personal Comm. from Scott Bryan); also see Richards (1958), Lee (1979), Kent and Frick (1984), Thiel and Gutow (2004) for related discussion] that have been suspended after being deposited on surrounding shores and riverbanks following their initial eruptions tens to hundreds of years ago (**Section 4** for the potential processes). This is a new, novel physical process that has not been fully documented before, especially in the modern/satellite era. Our analysis is the first study, to the best of our knowledge, to carefully document the secondary raft process on timescales of years or longer using satellite imagery, further validating the importance of this process as suggested by previous studies (Pullar et al., 1977; Osborne et al., 1991; Shane et al., 1998; Bryan et al., 2012; Jutzeler et al., 2014). This secondary raft process is likely relevant for the dispersal of eruptive products from many volcanic systems in coastal regions (e.g., Krakatau in Indonesia, Tonga-Fiji region). Although the secondary rafts are much smaller scale individually compared to large pumice rafts associated with new eruptions such as the Havre 2012 and the Krakatau 1883 eruption, they can be much more frequent. Thus, they may potentially still be important for material transport and local/regional scale biology. We acknowledge that a systematic analysis of secondary rafts on regional/global scales is needed to quantify this effect (if any). Without any specimens of the pumice that we detected, we are presently unable to ascertain a specific source eruption of the rafts. In addition, even with samples, it may still be difficult to determine the original source eruption or eruptions, as pumice material from the 1878 eruption and subsequent eruptions have very similar overall composition and texture (Bernard and Bouvet de Maisonneuve, 2020). However, the morphology of the pumice samples (angular vs. rounded, presence of biological material) can at least provide some constraints on whether the pumice represents a new eruption or remobilized material (from Rabaul or other farther eruptions, based on composition).

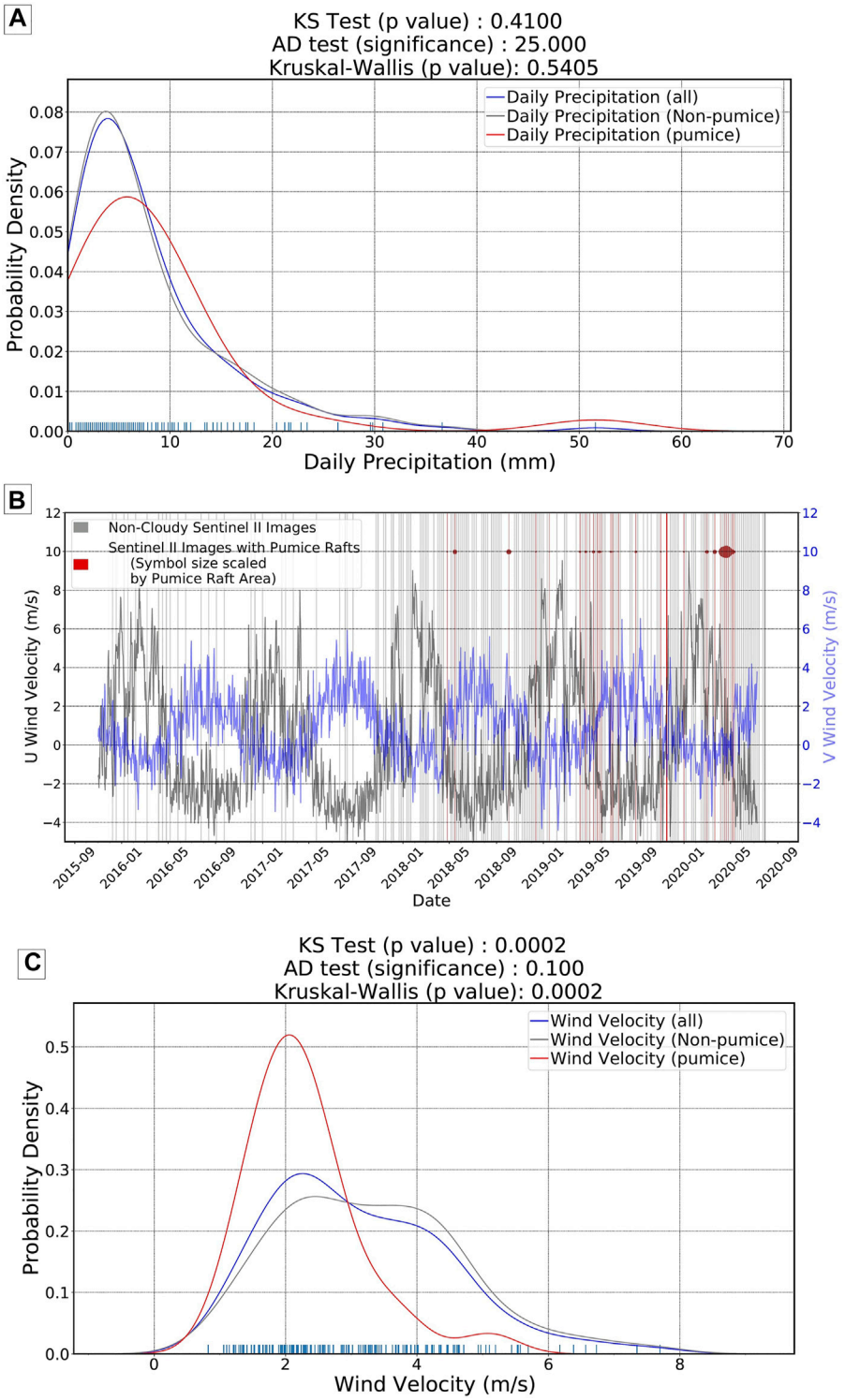

FIGURE 4 | (A) Probability density function for the daily precipitation in the Rabaul region (5 days rolling window) **(B)** Time series of daily wind directionality in the Rabaul region—U wind velocity is the eastward component of wind while the V wind velocity is the northward component **(C)** Probability density function for daily wind magnitude in the Rabaul region (5 days rolling window).

Furthermore, field work in the Rabaul region can ground truth our conclusions and help test whether there is enough erodible material in the coastal areas to form rafts.

4 DISCUSSION

4.1 Source of Pumice Remobilization: Influence of Weather Factors

Considering our interpretation that the detected rafts in Rabaul are secondary rafts, an important question to consider is what potential physical mechanisms are responsible for the mobilization of pumiceous material. One possibility is that resuspension is a consequence of local climatological conditions, e.g., high rainfall events, high wind conditions that dislodge pumice along coastlines and riverbanks back into the water. Local weather can lead to landslides and dislodgement of small pumice rafts [e.g., local pumice raft from rockslide in the Askja caldera, Iceland on 21 July 2014 (Icelandic Meteorological, 2014)]. Using ERA5 Daily Aggregate Reanalysis Product (Hersbach et al., 2020) (directly accessible through GEE), we generated time series of various atmospheric properties—daily mean air temperature, wind magnitude, wind direction, and precipitation. These time series were all sampled from the same location, directly on top of one of Rabaul's vents, and the time series spanned the entire Sentinel-2 coverage period in the area. We did not observe any significant correlation between the daily mean air temperature and the detection of pumice rafts in the area (**Supplementary Figure S3**). We also explored potential correlations with weather parameters up to 10 days before raft detection to allow for some unknown advection time (**Supplementary Data**). Overall, we did not find significantly different results across these windows. The main statistically robust relationships in our dataset are between raft detection and wind and precipitation.

4.1.1 Precipitation

To compare the impact of wind, precipitation, and other weather parameters on raft detection, we construct and compare probability density distributions (PDF). A PDF is a function that provides the relative likelihood of an event (raft detection) given another parameter (e.g. wind speed, recorded rainfall). We find that the PDF for the days with sighted pumice rafts (red curve, **Figure 4A**) were slightly different from the curves for the total days in the coverage period (blue curve, **Figure 4A**) and the days where no rafts were detected (gray curve, **Figure 4A**) (using 5 day rolling window, other windows have similar results). However, this difference is not statistically significant when using either the Anderson-Darling (AD) test statistic (Scholz and Stephens, 1987) or the Epps-Singleton (ES) test statistic (Epps and Singleton, 1986). The medians of the raft vs. non-raft precipitation PDFs are potentially different, as shown by the lower p-value for the Kruskal-Wallis test (Kruskal and Wallis, 1952). We also do not find any clear correlation between precipitation values and raft area.

We analyzed the long-term precipitation history in the Rabaul area to help elucidate the remobilization process. We used ERA5 data to consider 3-day rolling sums of precipitation values in Rabaul since 1990. From the long-term history, we observe the peak precipitation occurred in February 2018. All of our detected rafts in Sentinel-2 imagery are post 2018 (further analysis using Landsat imagery is included in **Supplementary Text S15**). This may be a consequence of increased frequency of sampling in the Rabaul area after the second Sentinel-2 satellite launch in March of 2017. Alternatively, the detection of rafts after the precipitation peak in early 2018 suggests that a large storm or significant weather event made rafts easier to remobilize post-2017. More detailed work, especially in the field in Rabaul, is needed to test these hypothesis and ascertain which coastal areas have significant amounts of pumice ready to mobilize.

Overall, we find that there is only a weak correlation between precipitation and raft detection. We posit that the slightly higher values for precipitation before raft detection compared to non-raft days suggest a role for higher precipitation to increase erosion and consequently encourage raft remobilization. However, it is clear that precipitation is not a unique factor since days of high precipitation are not always followed by raft detections (**Figure 4A**, **Supplementary Figure S2**).

4.1.2 Wind

In addition to precipitation, we also considered the role of wind in raft formation. **Figure 4B** shows the daily wind direction [U (eastward), V (northward) components] in Rabaul along with red vertical lines highlighting days with raft detections. We find that the general wind direction in Rabaul has a strong seasonal cycle which is relatively stable over the past 5 years. Interestingly, most of our pumice raft sightings were around the March–May window despite having a number of non-cloudy images for other months. This suggests that there is some seasonality to the raft remobilization process.

In order to assess the role of overall wind magnitude, we show the probability distribution curves for wind velocity for all days in the Sentinel-2 coverage period (blue curve, **Figure 4C**), days without raft sightings (gray curve, **Figure 4C**), and days with raft sightings (red curve, **Figure 4C**) (using 5 day rolling window, other windows have similar results). We find that days where rafts were detected produced a significantly different probability distribution curve (**Figure 4C**). There is also a high correlation between wind amplitude and raft area (**Supplementary Figure S3**). However, since there are not many high raft area data points, the correlation may be biased by outliers. Overall, we see most of our raft sightings are in the distinct range of wind velocities (1 to 4 m/s) compared to the overall distribution. Even when accounting for different sample sizes, this difference is statically significant [Anderson-Darling (AD) test statistic (Scholz and Stephens, 1987); the Epps-Singleton (ES) test statistic (Epps and Singleton, 1986); Kolmogorov-Smirnov (KS) test (Hodges, 1958)]. We conclude that the high wind velocities likely break up and disperse the secondary rafts too rapidly for Sentinel-2 to capture. We would note that there are number of non-cloudy days with low wind velocity and no raft detection (**Figure 4C**, grey curve). Thus, wind condition is not the only parameter that controls the temporal pattern of raft detection with an additional role of seasonality.

4.2 Open Challenges for Global Pumice Detection Algorithm

Although our ML algorithm is reasonably successful for pumice raft detection, it is not fully automated. The classification process requires manual checks to filter out incorrect classifications of pumice and cloud cover. In particular, the light cloud cover with a flat spectral response curve can at times be misclassified as pumice (and vice versa). Also, the satellite's viewing geometry may create a "Sun glint" in certain images, where all of the pixels in the RGB rendering are affected and off-colored. The classifier subsequently has difficulty correctly identifying the correct class of each pixel. There are some ways these issues can be addressed. Better atmospheric corrected products, specifically for oceanic regions, would help improve detection. For instance, in some cases, using the atmosphere corrected Surface Reflectance (Level-2A) product can allow us to detect pumice rafts on images discolored due to atmospheric effects (**Supplementary Figure S10**). Alternatively, more stringent data filtering for satellite viewing angle and cloudiness bounds can help reduce potential false positives. Finally, incorporating additional satellite imagery data e.g., geostationary imagery with high temporal frequency (more detailed raft tracking as well as better cloud detection based on motion) and radar imagery (sensitive to surface roughness and reduced sensitivity to atmospheric effects) could help improve detection accuracy. Additional potential options for algorithmic improvement are described in **Supplementary Text S11**.

5 CONCLUSION

In this study, we show that GEE and RF classifiers can be successfully used to detect pumice rafts. This can be useful to efficiently track pumice rafts, which can pose as hazards and disruptions to boats and harbors (Jutzeler et al., 2014; Jutzeler et al., 2020) and thus help with hazard mitigation and coordination services along populated shorelines (e.g., ongoing raft arrival on mainland Japan from the August 2021 eruption of Fukutoku-Okanoba volcano). Our methodology can help address our current strong bias in eruption detection and improve the detection of submarine eruptions globally. Using GEE removes the large data storage requirement and allows for a semi-automated, easily scalable classification with minimal subjective biases. Using the Rabaul caldera regions in Papua New Guinea as a case study, we show that not all detected pumice rafts necessarily correlate with a new eruption. Indeed, in some coastal regions, remobilization is likely to be a widespread phenomenon and can affect the spatial pattern of how products from an eruption are deposited as well as pumice remobilization after large storms/coastal tsunamis (e.g., Anak Krakatau 2018; Hunga Tonga Hunga Ha'apai 2022 eruption). Since these spatial patterns serve as the basis for estimating volcanic eruptive volumes, as well as long-distance (on tens to hundreds of kilometers scale) stratigraphic correlations (Shane et al., 1998; Mouginis-Mark and Zimbelman, 2020; Freundt et al., 2021), the raft remobilization process needs to be further analyzed. Finally, if drifting, remobilized pumice is common, its presence can impact the detection of future submarine eruptions, especially small eruptions in near coastal regions. Thus understanding the morphology, abrasion, and lifetime of the remobilized rafts (i.e., how they fragment over time and any differences from newly erupted rafts) is critical to remove this false positive for new eruption detection.

DATA AVAILABILITY STATEMENT

The original contributions presented in the study are publicly available. This data can be found here: https://figshare.com/projects/Pumice_Raft_Detection_Using_Machine-Learning_on_Multispectral_Satellite_Imagery/126466.

AUTHOR CONTRIBUTIONS

TM and MZ conceived the study and were in charge of overall direction and planning. MZ wrote the algorithm scripts and applied algorithm in case study. TM and MZ analysed the data and wrote the manuscript with input from all authors.

ACKNOWLEDGMENTS

We thank Amber Madden-Nadeau, Samantha L. Engwell, Sebastian Watt, Michael Cassidy, Ralf Bennartz, Ashok Gupta, Liam Kelly, John Rausch for useful discussions and suggestions for the manuscript text. We thank the editor and the reviewers for their valuable comments and suggestions. We thank Planet Labs, Sentinel-2, Landsat 7/8, and Google Earth Engine platform for providing the satellite imagery and computational tools. MZ acknowledges support from the MIT UROP program, TM acknowledges funding support from the Crosby Postdoc Fellowship at MIT, and KF acknowledges funding support from the NASA Grant 80NSSC20K1450.

SUPPLEMENTARY MATERIAL

The Supplementary Material for this article can be found online at: https://www.frontiersin.org/articles/10.3389/feart.2022.838532/full#supplementary-material

REFERENCES

Baker, E. T., Lavelle, J. W., Feely, R. A., Massoth, G. J., Walker, S. L., and Lupton, J. E. (1989). Episodic Venting of Hydrothermal Fluids From the Juan de Fuca Ridge. *J. Geophys. Res.* 94, 9237–9250. doi:10.1029/jb094ib07p09237

Bernard, O., and Bouvet de Maisonneuve, C. (2020). Controls on Eruption Style at Rabaul, Papua New Guinea - Insights from Microlites, Porosity and Permeability Measurements. *J. Volcanology Geothermal Res.* 406, 107068. doi:10.1016/j.jvolgeores.2020.107068

Biermann, L., Clewley, D., Martinez-Vicente, V., and Topouzelis, K. (2020). Finding Plastic Patches in Coastal Waters Using Optical Satellite Data. *Sci. Rep.* 10, 5364. doi:10.1038/s41598-020-62298-z

Brandl, P. A., Schmid, F., Augustin, N., Grevemeyer, I., Arculus, R. J., Devey, C. W., et al. (2020). The 6-8 Aug 2019 Eruption of 'Volcano F' in the Tofua Arc, Tonga. *J. Volcanology Geothermal Res.* 390, 106695. doi:10.1016/j.jvolgeores.2019.106695

Brasier, M. D., Matthewman, R., McMahon, S., and Wacey, D. (2011). Pumice as a Remarkable Substrate for the Origin of Life. *Astrobiology* 11, 725–735. doi:10.1089/ast.2010.0546

Brenot, H., Theys, N., Clarisse, L., van Geffen, J., van Gent, J., Van Roozendael, M., et al. (2014). Support to Aviation Control Service (SACS): an Online Service for Near-Real-Time Satellite Monitoring of Volcanic Plumes. *Nat. Hazards Earth Syst. Sci.* 14, 1099–1123. doi:10.5194/nhess-14-1099-2014

Bryan, S. E., Cook, A., Evans, J. P., Colls, P. W., Wells, M. G., Lawrence, M. G., et al. (2004). Pumice Rafting and Faunal Dispersion during 2001-2002 in the Southwest Pacific: Record of a Dacitic Submarine Explosive Eruption from Tonga. *Earth Planet. Sci. Lett.* 227, 135–154. doi:10.1016/j.epsl.2004.08.009

Bryan, S. E., Cook, A. G., Evans, J. P., Hebden, K., Hurrey, L., Colls, P., et al. (2012). Rapid, Long-Distance Dispersal by Pumice Rafting. *PloS one* 7, e40583. doi:10.1371/journal.pone.0040583

Cesca, S., Letort, J., Razafindrakoto, H. N. T., Heimann, S., Rivalta, E., Isken, M. P., et al. (2020). Drainage of a Deep Magma Reservoir Near Mayotte Inferred from Seismicity and Deformation. *Nat. Geosci.* 13, 87–93. doi:10.1038/s41561-019-0505-5

Del Bello, E., Taddeucci, J., Merrison, J. P., Rasmussen, K. R., Andronico, D., Ricci, T., et al. (2021). Field-Based Measurements of Volcanic Ash Resuspension by Wind. *Earth Planet. Sci. Lett.* 554, 116684. doi:10.1016/j.epsl.2020.116684

DeVantier, L. (1992). Rafting of Tropical Marine Organisms on Buoyant Corolla. *Mar. Ecol. Prog. Ser.* 86, 301–302. doi:10.3354/meps086301

Embley, R. W., Baker, E. T., Chadwick, W. W., Lupton, J. E., Resing, J. A., Massoth, G. J., et al. (2004). Explorations of Mariana Arc Volcanoes Reveal New Hydrothermal Systems. *Eos Trans. AGU* 85, 37–40. doi:10.1029/2004eo040001

Engwell, S., Mastin, L., Tupper, A., Kibler, J., Acethorp, P., Lord, G., et al. (2021). Near-real-time Volcanic Cloud Monitoring: Insights into Global Explosive Volcanic Eruptive Activity through Analysis of Volcanic Ash Advisories. *Bull. Volcanology* 83, 1–17. doi:10.1007/s00445-020-01419-y

Epps, T. W., and Singleton, K. J. (1986). An Omnibus Test for the Two-Sample Problem Using the Empirical Characteristic Function. *J. Stat. Comput. Simulation* 26, 177–203. doi:10.1080/00949658608810963

Erupt (2017). *Volcanic Eruptions and Their Repose, Unrest, Precursors, and Timing*. Washington, DC: The National Academies Press. doi:10.17226/24650

Etyemezian, V., Gillies, J. A., Mastin, L. G., Crawford, A., Hasson, R., Van Eaton, A. R., et al. (2019). Laboratory Experiments of Volcanic Ash Resuspension by Wind. *J. Geophys. Res. Atmos.* 124, 9534–9560. doi:10.1029/2018jd030076

Fauria, K., Jutzeler, M., Mittal, T., Gupta, A., Kelly, L., Rausch, J., et al. (2022). Simultaneous Creation of a Large Vapor Plume and Pumice Raft by a Shallow Submarine Eruption. *Earth Space Sci. Open Archive*. doi:10.1002/essoar.10510412.1

Freundt, A., Schindlbeck-Belo, J. C., Kutterolf, S., and Hopkins, J. L. (2021). *Tephra Layers in the Marine Environment: A Review of Properties and Emplacement Processes*. London: Geological Society. *Special Publications* 520.

Furtney, M. A., Pritchard, M. E., Biggs, J., Carn, S. A., Ebmeier, S. K., Jay, J. A., et al. (2018). Synthesizing Multi-Sensor, Multi-Satellite, Multi-Decadal Datasets for Global Volcano Monitoring. *J. Volcanology Geothermal Res.* 365, 38–56. doi:10.1016/j.jvolgeores.2018.10.002

Gorelick, N., Hancher, M., Dixon, M., Ilyushchenko, S., Thau, D., and Moore, R. (2017). Google Earth Engine: Planetary-Scale Geospatial Analysis for Everyone. *Remote sensing Environ.* 202, 18–27. doi:10.1016/j.rse.2017.06.031

Global Volcanism Program (2013). "Global Volcanism Program," in *Volcanoes of the World*. Editor E. Venzke (Smithsonian Institution), 2, 4–6. doi:10.5479/si.GVP.VOTW4-2013

Gvp (1994). "Report on Rabaul (Papua New Guinea)," in *Bulletin of the Global Volcanism Network*. Editor R. Wunderman (Smithsonian Institution), 19, 8. doi:10.5479/si.GVP.BGVN199408-252140

Gvp (2006). "Report on Rabaul (Papua New Guinea),". Editor R. Wunderman (Smithsonian Institution), 31, 9. doi:10.5479/si.GVP.BGVN200609-252140*Bull. Glob. volcanism Netw.*

Heaney, K. D., Campbell, R. L., and Snellen, M. (2013). Long Range Acoustic Measurements of an Undersea Volcano. *The J. Acoust. Soc. America* 134, 3299–3306. doi:10.1121/1.4818844

Hersbach, H., Bell, B., Berrisford, P., Hirahara, S., Horányi, A., Muñoz-Sabater, J., et al. (2020). The ERA5 Global Reanalysis. *Q.J.R. Meteorol. Soc.* 146, 1999–2049. doi:10.1002/qj.3803

Hodges, J. L. (1958). The Significance Probability of the Smirnov Two-Sample Test. *Ark. Mat.* 3, 469–486. doi:10.1007/bf02589501

Icelandic Meteorological Office (2014). *Rockslide in Askja, July 21 2014 - Preliminary Results of Observations*.

Jutzeler, M., Marsh, R., Carey, R. J., White, J. D., Talling, P. J., and Karlstrom, L. (2014). On the Fate of Pumice Rafts Formed during the 2012 Havre Submarine Eruption. *Nat. Commun.* 5, 3660. doi:10.1038/ncomms4660

Jutzeler, M., Marsh, R., van Sebille, E., Mittal, T., Carey, R. J., Fauria, K. E., et al. (2020). Ongoing Dispersal of the 7 August 2019 Pumice Raft from the Tonga Arc in the Southwestern Pacific Ocean. *Geophys. Res. Lett.* 47, e1701121. doi:10.1029/2019gl086768

Kelley, D. (2017). Volcanology: Vulcan Rule beneath the Sea. *Nat. Geosci.* 10, 251–253. doi:10.1038/ngeo2929

Kent, L., and Frick, C. (1984). Drift Pumice in the Indian and South Atlantic Oceans. *South. Afr. J. Geology.* 87, 19–33.

Kruskal, W. H., and Wallis, W. A. (1952). Use of Ranks in One-Criterion Variance Analysis. *J. Am. Stat. Assoc.* 47, 583–621. doi:10.1080/01621459.1952.10483441

Lee, V. F. (1979). Maritime Pseudoscorpions of Baja California, Mexico (Arachnida: Pseudoscorpionida).

Mandeville, C. W., Carey, S., and Sigurdsson, H. (1996). Sedimentology of the Krakatau 1883 Submarine Pyroclastic Deposits. *Bull. Volcanol* 57, 512–529. doi:10.1007/BF00304436

Manville, V., Segschneider, B., and White, J. D. L. (2002). Hydrodynamic Behaviour of Taupo 1800a Pumice: Implications for the Sedimentology of Remobilized Pyroclasts. *Sedimentology* 49, 955–976. doi:10.1046/j.1365-3091.2002.00485.x

Matsumoto, H., Zampolli, M., Haralabus, G., Stanley, J., Mattila, J., and Meral Özel, N. (2019). Interpretation of Detections of Volcanic Activity at Ioto Island Obtained from *In Situ* Seismometers and Remote Hydrophones of the International Monitoring System. *Sci. Rep.* 9, 19519. doi:10.1038/s41598-019-55918-w

Mittal, T., and Delbridge, B. (2019). Detection of the 2012 Havre Submarine Eruption Plume Using Argo Floats and its Implications for Ocean Dynamics. *Earth Planet. Sci. Lett.* 511, 105–116. doi:10.1016/j.epsl.2019.01.035

Mouginis-Mark, P. J., and Zimbelman, J. R. (2020). Rafted Pumice: A New Model for the Formation of the Medusae Fossae Formation, Mars. *Icarus* 343, 113684. doi:10.1016/j.icarus.2020.113684

Ochoa, C. N. (2009). *Report of Drift Pumice Near Socorro Island (25 January to 3 February 2009)*.

O'Malley, R. T., Behrenfeld, M. J., Westberry, T. K., Milligan, A. J., Reese, D. C., and Halsey, K. H. (2014). Improbability Mapping: a Metric for Satellite-Detection of Submarine Volcanic Eruptions. *Remote sensing Environ.* 140, 596–603.

Osborne, N. M., Enright, N. J., and Parnell, K. E. (1991). The Age and Stratigraphic Significance of Sea-Rafted Loisels Pumice in Northern New Zealand. *J. R. Soc. New Zealand* 21, 357–371. doi:10.1080/03036758.1991.10420833

Park, C., and Schmincke, H.-U. (2020). Multistage Damming of the Rhine River by Tephra Fallout during the 12,900 Bp Plinian Laacher See Eruption (germany). Syn-Eruptive Rhine Damming I. *J. Volcanology Geothermal Res.* 389, 106688. doi:10.1016/j.jvolgeores.2019.106688

Planet Team (2021). "Planet Application Program Interface," in *Space for Life on Earth*.

Poland, M. P., Lopez, T., Wright, R., and Pavolonis, M. J. (2020). Forecasting, Detecting, and Tracking Volcanic Eruptions from Space. *Remote Sens Earth Syst. Sci.* 3, 55–94. doi:10.1007/s41976-020-00034-x

Pullar, W. A., Kohn, B. P., and Cox, J. E. (1977). Air-Fall Kaharoa Ash and Taupo Pumice, and Sea-Rafted Loisels Pumice, Taupo Pumice, and Leigh Pumice in Northern and Eastern Parts of the North Island, New Zealand. *New Zealand Journal Geology. Geophysics* 20, 697–717. doi:10.1080/00288306.1977.10430729

Qi, L., Hu, C., Mikelsons, K., Wang, M., Lance, V., Sun, S., et al. (2020). In Search of Floating Algae and Other Organisms in Global Oceans and Lakes. *Remote Sensing Environ.* 239, 111659. doi:10.1016/j.rse.2020.111659

Richards, A. F. (1958). Transpacific Distribution of Floating Pumice from Isla San Benedicto, Mexico. *Deep Sea Res. (1953)* 5, 29–35. doi:10.1016/S0146-6291(58)80005-3

Risso, C., Scasso, R. A., and Aparicio, A. (2002). Presence of Large Pumice Blocks on Tierra Del Fuego and South Shetland Islands Shorelines, From 1962 South Sandwich Islands Eruption. *Mar. Geology.* 186, 413–422. doi:10.1016/s0025-3227(02)00190-1

Rubin, K., Soule, S. A., Chadwick, W., Jr, Fornari, D., Clague, D., Embley, R., et al. (2012). Volcanic Eruptions in the Deep Sea. *oceanog* 25, 142–157. doi:10.5670/oceanog.2012.12

Sakuno, Y. (2021). Trial of Chemical Composition Estimation Related to Submarine Volcano Activity Using Discolored Seawater Color Data Obtained from GCOM-C SGLI. A Case Study of Nishinoshima Island, Japan, in 2020. *Water* 13, 1100. doi:10.3390/w13081100

Santana-Casiano, J. M., González-Dávila, M., Fraile-Nuez, E., De Armas, D., González, A. G., Domínguez-Yanes, J. F., et al. (2013). The Natural Ocean Acidification and Fertilization Event Caused by the Submarine Eruption of El Hierro. *Sci. Rep.* 3, 1140. doi:10.1038/srep01140

Scholz, F. W., and Stephens, M. A. (1987). K-Sample Anderson-Darling Tests. *J. Am. Stat. Assoc.* 82, 918–924. doi:10.1080/01621459.1987.10478517

Shane, P., Froggatt, P., Smith, I., and Gregory, M. (1998). Multiple Sources for Sea-Rafted Loisels Pumice, New Zealand. *Quat. Res.* 49, 271–279. doi:10.1006/qres.1998.1968

Tepp, G., Chadwick, W. W., Jr, Haney, M. M., Lyons, J. J., Dziak, R. P., Merle, S. G., et al. (2019). Hydroacoustic, Seismic, and Bathymetric Observations of the 2014 Submarine Eruption at Ahyi Seamount, Mariana Arc. *Geochem. Geophys. Geosyst.* 20, 3608–3627. doi:10.1029/2019gc008311

Tepp, G., and Dziak, R. P. (2021). The Seismo-Acoustics of Submarine Volcanic Eruptions. *J. Geophys. Res. Solid Earth* 126, e2020JB020912. doi:10.1029/2020jb020912

Thiel, M., and Gutow, L. (2004). The Ecology of Rafting in the Marine Environment. I. The Floating Substrata. *Oceanography Mar. Biol. Annu. Rev.* 42, 181–263. doi:10.1201/9780203507810.ch6

Tilstone, G. H., Miller, P. I., Brewin, R. J. W., and Priede, I. G. (2014). Enhancement of Primary Production in the North Atlantic Outside of the Spring Bloom, Identified by Remote Sensing of Ocean Colour and Temperature. *Remote sensing Environ.* 146, 77–86. doi:10.1016/j.rse.2013.04.021

Torres, R. C., Self, S., Martinez, M. M. L., Newhall, C., and Punongbayan, R. (1996). *Secondary Pyroclastic Flows from the June 15, 1991, Ignimbrite of Mount Pinatubo Fire and Mud: Eruptions and Lahars of Mount Pinatubo*. Philippines, 665–678.

White, J. D. L., Schipper, C. I., and Kano, K. (2015). "Submarine Explosive Eruptions," in *The Encyclopedia of Volcanoes*. Editor H. Sigurdsson. Second EditionSecond edition edn (Amsterdam: Academic Press), 553–569. doi:10.1016/B978-0-12-385938-9.00031-6

White, S. M., Crisp, J. A., and Spera, F. J. (2006). Long-term Volumetric Eruption Rates and Magma Budgets. *Geochem. Geophys. Geosystems* 7. doi:10.1029/2005gc001002

Whiteside, A., Dupouy, C., Singh, A., Frouin, R., Menkes, C., and Lefèvre, J. (2021). Automatic Detection of Optical Signatures within and Around Floating Tonga-Fiji Pumice Rafts Using MODIS, VIIRS, and OLCI Satellite Sensors. *Remote Sensing* 13, 501. doi:10.3390/rs13030501

Wilcock, W. S. D., Tolstoy, M., Waldhauser, F., Garcia, C., Tan, Y. J., Bohnenstiehl, D. R., et al. (2016). Seismic Constraints on Caldera Dynamics from the 2015 Axial Seamount Eruption. *Science* 354, 1395–1399. doi:10.1126/science.aah5563

Wright, R., Flynn, L. P., Garbeil, H., Harris, A. J. L., and Pilger, E. (2004). Modvolc: Near-Real-Time Thermal Monitoring of Global Volcanism. *J. Volcanology Geothermal Res.* 135, 29–49. doi:10.1016/j.jvolgeores.2003.12.008

Yoshida, K., Tamura, Y., Sato, T., Hanyu, T., Usui, Y., Chang, Q., et al. (2022). Variety of the Drift Pumice Clasts from the 2021 Fukutoku-Oka-no-Ba Eruption, Japan. *Isl. Arc* 31. doi:10.1111/iar.12441

Conflict of Interest: The authors declare that the research was conducted in the absence of any commercial or financial relationships that could be construed as a potential conflict of interest.

Supplementary Material

1 SUPPLEMENTARY DATA

Text S1. - Other Raft Detection Algorithms In addition to ML algorithms, we tried other spectral index or simple rule-based algorithms for raft detection. For instance, we set bounded ranges for the measured brightness Sentinel-2 spectral bands, based on our calculated spectral response curves. We found that this algorithm could differentiate between pumice and non-pumice pixels in a single image for a chosen day and time. However, when applied to different geo-temporal areas, this method required significant adjustment each time for good accuracy. Similarly, we found that an algorithm just using spectral indices to emphasize specific characteristics of the spectra was not as robust as our final ML algorithm.

Text S2. - Raft Morphology In order to assess whether there is any clear visual morphological difference between new vs. older, remobilized pumice rafts, we analyzed the raft morphology compared to rafts from the new 2019 eruption in the Tonga area (Supplement Figure S5, Planet Labs Imagery). The Tonga raft image from September 6, 2019, was taken about a month after the eruption, and shows that the raft has significantly dispersed from its initial shape (Jutzeler et al., 2020, See Figure 2A). Nevertheless, the Tonga rafts are morphologically distinct from the Rabaul rafts (Some images from March-April 2020, Supplement Figure S5). Although both the rafts interact with the ocean eddies and surface wind stresses, only the pumice concentration pattern for only the Tonga rafts have a distinctive sharp trailing edge and a diaper-tail shaped concentrated region. Instead, the Rabaul rafts trend toward longer, more diffusive-type formations with several smaller, disconnected strands. Since the interaction of pumice rafts with ocean and surface wind dynamics is not well-understood (Jutzeler et al., 2020), we do not have a clear physical understanding of why these differences occur. We hypothesize that the morphological differences may due to the rounding of pumice particles in re-suspended rafts due to more prolonged exposure to wave motion and/or surface erosion. Additionally, the pumice particle sizes in the re-suspended rafts may differ from the Tonga raft due to either different eruptive dynamics or preferential selection of a certain pumice size class during the re-suspension process. Based on related work on the interaction of buoyant particles (e.g., Marine litter, Sargassum) with the ocean eddies and wind-driven Langmuir circulation (Thorpe, 2004; Van Sebille et al., 2020; Chang et al., 2019; Miron et al., 2020; Beron-Vera, 2020), we expect the differences in shape and size of pumice to have a significant impact on the raft morphology. It is also surprising that the re-rafted pumice remains buoyant for extended periods at the ocean's surface, despite the weathering and erosion. The two potential mechanisms for explaining the long flotation times for pumice rafts, in general, are gas trapping by water within the pumice and gas-filled isolated porosity (Fauria et al., 2017). Since these processes' efficiency is directly related to the pumice micro-structure, a detailed analysis of the re-rafted Rabaul pumice can test if these mechanisms can explain the frequent raft re-suspension in this region.

Text S3. - Detection of Discolored Water While our study focuses primarily on detecting pumice rafts, we included classes for discolored water as another signature for submarine volcanic eruptions. Our algorithm is moderately successful at detecting discolored water, as illustrated by a classified image from the Kavachi submarine volcano (Supplement Fig S1, we do not fully match the true extents of the hydrothermal plume). However, we found that the detection of these classes is more challenging than pumice rafts. Since discolored water physically represents a mixture of hydrothermal fluids/suspended material with seawater, there is less distinction between the spectral characteristics of the discolored and normal water. Additional work potentially using more input features for ML algorithms is required to improve detection accuracy and robustness. For instance, some two/three-band spectral indices can be included as input features (Qi

et al., 2020). Although we found that using spectral index alone did not result in a robust classifier, a thorough examination combining spectral indexes and full reflectance data would likely help improve the detection. Additional datasets outside of Sentinel-2 (e.g., chlorophyll ocean color and fluorescence line heights) can potentially be included to improve the accuracy of the ML algorithm (Whiteside et al., 2021) and distinguish between discolored water and plankton blooms in response to an influx of nutrients (Wilson et al., 2019; Black et al., 2020; Qi et al., 2020; Kritten et al., 2020).

Text S4. - Algorithm Details Since we are interested in developing an algorithm that can be applied to different geo-temporal areas without significant user adjustment, we used Machine Learning (ML) algorithms due to their significant success in image classification (Abburu and Golla, 2015). ML algorithms can be automated, non-linear, iteratively improved, and easily scaled to extensive data collections. This makes them reasonable candidates for our scientific goal of detecting pumice rafts globally. Specifically, we used the GEE-provided Random Forest (RF) classifier to classify the image pixels (Fig 1C). RF classifiers build multiple decision trees, each based on a randomly selected subset of possible input parameters (here spectral bands). Each tree then classifies a pixel based upon its unique set of branches, and finally, a majority vote is passed to decide the final classification for the pixel (Belgiu and Drăguţ, 2016). Our algorithm used an RF classifier with 32 trees since it empirically provided a good, stable classification algorithm and robustness against overfitting. Since the RF algorithm is already implemented in the GEE platform, it is easy to query any Sentinel-2 image and return a classified image. Each class is highlighted in a specified color (See GEE Scripts provided with the manuscript for specific examples).

Text S5. - Algorithm Validation To evaluate method accuracy, we can construct a confusion matrix using a set of validation data. Confusion matrices compare predicted values against the validation or known values and thus are used to calculate performance metrics for classification algorithms, such as misclassification rate and accuracy. The validation set was constructed by manually demarcating areas of pixels that were not used to train the classifier and labelling each area as the appropriate class. Then, corresponding pixels from the originally classified are sampled and compared to the validation set of pixels. A confusion matrix is constructed based on how many of the classified pixels match the validation pixels. For our main training area in Rabaul on April 20, 2020 (Fig 2B), the confusion matrix returns an accuracy of 0.9164 (Supplementary Figure S7). This indicates that around 91% of the pixels were classified into the same category as our validation set. The high accuracy is a good indicator that our algorithm can automatedly detect and trace rafts.

Text S6. - Sentinel-2 Product The Multi-Spectral Instrument (MSI) onboard Sentinel-2 collects data from 13 different spectral bands at varying resolutions, and GEE offers two different data products for Sentinel-2 — Top-of-Atmosphere and Surface Reflectance. Since the Surface Reflectance collection typically processes the MSI data assuming land reflectance values rather than ocean values, we used the Level-1C Top-of-Atmosphere Reflectance product. We note that Sentinel-2's spectral bands are similar to several other Earth observing satellites, particularly Landsat-8 and Landsat-7. Thus, we anticipate that the methodology and algorithm developed in this study can be transferred to Landsat data products.

Text S7. - Algorithm Application Details Before applying the algorithm, we applied a land mask. As we are focusing only on signatures of underwater eruptions that are found in water, we could disregard every images' land pixels. Thus, we masked the land pixels in the images using data from the Global Surface Water dataset, a high-resolution dataset that shows the location and spread of surface water from 1984-2015 (Pekel et al., 2016). Using this land mask effectively removed the land pixels from consideration by the algorithm. The land mask could be used in most areas, but it could sometimes not be employed in the Tonga region due to small islands and atolls. We manually filtered the classified image to remove any land

pixels misidentified as pumice rafts in these cases. Due to inherent computational limits for GEE accounts, the algorithm was applied to month or half-a-month long intervals of time with sufficient resolution to see where the classifier marked out pumice (see the scripts for examples). After image classification, pumice rafts were identified through manual review of the classified images.

Text S8. - Rabaul Eruption History Since the last caldera forming eruption, the volcanic activity has built up multiple vents encircling the bay, including the historically very active Vulcan and Tavurvur vents (See Figure 3A, large compositional range from basalt to dacite). The low-lying Rabaul caldera's outer flanks are composed of thick tuff from pyroclastic-flows deposited during the caldera-forming Plinian eruptions (GVP, 2006). Since the town of Rabaul is located nearby, volcanic activity in the area is nominally well-recorded. In 1878, twin eruptions of both the Tavurvur and Vulcan vents generated a large pumice raft that was large enough to form an island and cover the neighboring bay (Bernard and Bouvet de Maisonneuve, 2020). In 1937, the early stage of an eruption at Vulcan killed 507 people and built up a cone such that Vulcan island was connected to the mainland (Bernard and Bouvet de Maisonneuve, 2020). Shortly after, Tavurvur also erupted, albeit in a series of smaller events (Bernard and Bouvet de Maisonneuve, 2020). Both vents produced pumices, and the samples from this 1937 twin eruption are extremely similar to those collected from the 1878 eruption (Bernard and Bouvet de Maisonneuve, 2020). Rabaul also has a history of more recent pumice raft formation. While the eruption in 2006 (Tavurvur vent) produced a small raft and the eruption in 2014 (Tavurvur vent) deposited pumices in the area (Bernard and Bouvet de Maisonneuve, 2020), the last major raft-forming eruption was in 1994 (VEI 4 eruption; GVP, 1994b,a, 2006, a simultaneous eruption from Vulcan and Tavurvur vents). The 1994 large raft from the Vulcan vent covered the bay in front of town of Rabaul, with a maximum thickness of up to $\sim$ 1.5 m (GVP, 1994b). Since the 1994 twin eruption, there has been intermittent semi-continuous activity at the Vulcan and Tavurvur vents, but no activity has been recorded since the 2014 eruption (Tavurvur vent) (Bernard and Bouvet de Maisonneuve, 2020).

Text S9. - Discolored Water Classes Training samples for Discolored Water Type I (shown in turquoise in the classified images) were drawn from the discolored water emanating from around the Tavurvur vent of the Rabaul caldera, likely due to the interaction of hydrothermal fluids with ocean water (Baker et al., 2002). Training samples for Discolored Water Type II (shown in magenta in the classified images) was drawn from a river's mouth to the south of the pumice raft. Consequently, the magenta discolored water class is likely to be more sediment-rich, while the turquoise discolored water class is more likely to indicate the presence of hydrothermal fluids.

Text S10. - Further Opportunities in Other Satellite Products In our study, we have focused on Sentinel-2 due to its high resolution and revisit frequency. Sentinel-2 offers coverage that includes all coastal water extending up to 20 km from the shoreline, all islands with an area greater than 100 square kilometers, and all closed seas (Drusch et al., 2012). Thus, using our algorithm, pumice rafts can be detected globally within Sentinel-2's coverage areas. With some minor modifications, our new algorithm can be extended to include other satellites, such as Landsat-7/8, ASTER, MODIS, and some of the geostationary satellites (e.g., Himawari, GEOS). Including these other satellites will allow for greater spatial coverage area, faster revisits, and a longer total duration of available historical imagery. Using GEE as a tool makes this task numerically feasible and more viable for a global-scale analysis.

Text S11. - Further Potential Algorithm Improvements Including additional input features (e.g., spectral ratios, multi-band spectral indices) may help improve the accuracy of the algorithm and make it fully automated. Furthermore, more feature engineering is necessary for robust discolored water detection. This could potentially also include co-located (and close in time) data products from other satellite imagery such

as Chl concentration and SST from Sentinel-2 ($\sim$ 300 m/pixel) (e.g., Whiteside et al. (2021)). Another potential improvement involves normalizing the affected images based on expected "ocean water" pixels before being passed to the classifier. In addition, GEE offers image metadata, including the satellite's viewing geometry and the area's cloudy percentage data at the time of the image collection. Applying viewing angle and cloudiness bounds outside of which the algorithm fails can filter out un-classifiable images.

In addition, our present ML algorithm only uses pixel scale information for classification and does not use any information from neighboring pixels or physical expectations for the rafts' shapes. This information can be particularly useful when distinguishing between cloud cover and pumice rafts, where our present semi-automated algorithm has the most difficulty. Generally, the shapes of clouds and pumice rafts are significantly distinct from each other. In addition, clouds often occur as repetition of similar shapes, so clouds may be better distinguished with pattern recognition ML algorithms. This could provide a possible solution to differentiate between these cloud and pumice pixels by adding additional spatial features to the RF algorithms.

Text S12 - Planet Imagery Planet Labs offers very high resolution imagery ($\sim$3m/pixel) of the entire Earth with a very frequent revisit time (daily). While we use this high resolution imagery to more closely examine images of the rafts that our algorithm detects, we primarily focus on using GEE resources for our study, as very high resolution imagery (e.g., Planet Labs) is typically not publicly available without commercial licenses.

Text S13 - Puyehue-Cordón Caulle Rafts We compared the spectral response curves to those of pumice rafts floating in lakes near the Puyehue-Cordón Caulle volcano complex, located in Chile (Elser et al., 2015). These lake rafts were formed from a higher silica eruption than the ones likely to have produced the rafts in the Tonga and Rabaul regions. Sentinel-2 images were not available for the Puyehue-Cordón Caulle lake rafts, so Landsat 8 images were used instead. Landsat 8 does not have as fine coverage as Sentinel-2, so not all of the same wavelengths were available. We find that the spectra for the lake pumice is broadly consistent with the shape of the other rafts.

Text S14 - Use of Landsat and Planet Imagery: Other Eruption Signatures We manually checked each day our algorithm detected a raft, as well as surrounding days with lower resolution (Landsat 7, Landsat 8) as well as higher resolution imagery (Planet Labs), to check if the rafts are associated with any other eruptive signatures expected for shallow submarine eruptions (e.g., aerial plumes, discolored water). We did not find signatures of eruptions such as aerial plumes or ash fall. Although there was some discolored water (indicator of hydrothermal fluid mixing) around the volcano vent, we did not find a significant relationship between the raft's spatial location and discolored water, or between the spatial area of discolored water (as a proxy for hydrothermal activity intensity) and the size of the raft (Supplement Fig S9). In addition, we did not find any significant shallow seismic activity near the Rabaul area co-incident with raft detection (Bondár and Storchak, 2011). Thus, we interpret that the detected rafts are not actually products from a new submarine eruption.

Text S15 - Use of Landsat Imagery: Rabaul Raft Detections Outside of Sentinel II Coverage Period To examine whether the more sparse raft detections in the Rabaul area prior to 2018 was due to the precipitation history or the lower satellite coverage prior to the launch of the second Sentinel II, we used Landsat 7 and Landsat 8 imagery to assess images before 2018 (Hartpence, 2021; Goward et al., 2001; Roy et al., 2014). Landsat 7 and Landsat 8 offer lower resolution (30 m/pixel) and longer daily revisit frequency ($>$ 16 days). However, Landsat 7 and Landsat 8 have been active since 1999. From manually analyzing

series of Landsat images from the pre-Sentinel period, we found only a few raft images. Thus, we cannot say definitively whether the spike in raft detections using our algorithm starting in 2018 is more likely due to the increase in coverage after the second Sentinel-2 satellite launch rather than long-term precipitation patterns.

Text S16 - Pumiceous Material In this study, we do not have ground truth observations to confirm that the imaged rafts in Rabaul are actually of pumice, nor that there are readily available stores of "true" pumice along the coast - that is vesicular volcanic glass fragments with vesicularity >50-80% (e.g., Thomas et al. (1994)). Moderately vesicular (e.g., 30-50%) juvenile clasts can have temporary buoyancy and all produce short-lived rafts. For example small rafts have been associated with eruptions from Metis Shoal/Late'iki but these were short-lived because they made up of vesicular lava fragments with 30-40% vesicularity (e.g., Melson et al. (1970)) rather than being of true pumice. As we have not ground truth observations to confirm the composition of the imaged rafts in Rabaul, we will refer to these rafts as made up of pumiceous material. Also, in the text, we will use the term pumice in a broad sense to represent pumiceous material rather than just "true" pumice.

GEE Script Links Script Links with step by step instructions (also provided with Figshare as a static copy) :

- Spectral Curves– plots the mean and standard deviation of spectral response curves, `https://code.earthengine.google.com/878027cf43a77bae30bbacaf072e5451`
- Classifier– runs classification on either single images or filmstrips of multiple days, `https://code.earthengine.google.com/e63e4ea41701db7ea9d26cf6f54b5ecd`
- Climate Time Series– collects climate data (precipitation, wind, temp., etc.) over extended time period and generates plots `https://code.earthengine.google.com/e5fe72a393e61a0bd56e286751a64a59`

Figshare Link Static copy of the script links:

- `https://figshare.com/projects/Pumice_Raft_Detection_Using_Machine-Learning_on_Multispectral_Satellite_Imagery/126466`

2 SUPPLEMENTARY TABLES AND FIGURES

2.1 Figures

REFERENCES

Abburu, S. and Golla, S. B. (2015). Satellite image classification methods and techniques: A review. *International journal of computer applications* 119

Baker, E. T., Massoth, G. J., de Ronde, C. E., Lupton, J. E., and McInnes, B. I. (2002). Observations and sampling of an ongoing subsurface eruption of kavachi volcano, solomon islands, may 2000. *Geology* 30, 975–978

Belgiu, M. and Drăguţ, L. (2016). Random forest in remote sensing: A review of applications and future directions. *ISPRS journal of photogrammetry and remote sensing* 114, 24–31

Bernard, O. and Bouvet de Maisonneuve, C. (2020). Controls on eruption style at rabaul, papua new guinea – insights from microlites, porosity and permeability measurements. *Journal of Volcanology and Geothermal Research* 406, 107068. doi:https://doi.org/10.1016/j.jvolgeores.2020.107068

Beron-Vera, F. J. (2020). Nonlinear dynamics of inertial particles in the ocean: From drifters and floats to marine debris and sargassum. *Nonlinear Dynamics* , 1–26

Black, B., Mittal, T., Lingo, F., Walowski, K., and Hernandez, A. (2020). Assessing the environmental consequences of the generation and alteration of mafic volcaniclastic deposits during large igneous province emplacement. *Large Igneous Provinces: A Driver of Global Environmental and Biotic Changes* , 117–131

Bondár, I. and Storchak, D. (2011). Improved location procedures at the international seismological centre. *Geophysical Journal International* 186, 1220–1244

Chang, H., Huntley, H. S., Jr, A. K., Carlson, D. F., Mensa, J. A., Mehta, S., et al. (2019). Small-scale dispersion in the presence of langmuir circulation. *Journal of Physical Oceanography* 49, 3069–3085

Drusch, M., Del Bello, U., Carlier, S., Colin, O., Fernandez, V., Gascon, F., et al. (2012). Sentinel-2: Esa's optical high-resolution mission for gmes operational services. *Remote sensing of Environment* 120, 25–36

Elser, J. J., Bastidas Navarro, M., Corman, J. R., Emick, H., Kellom, M., Laspoumaderes, C., et al. (2015). Community structure and biogeochemical impacts of microbial life on floating pumice. *Applied and Environmental Microbiology* 81, 1542–1549

Fauria, K. E., Manga, M., and Wei, Z. (2017). Trapped bubbles keep pumice afloat and gas diffusion makes pumice sink. *Earth and Planetary Science Letters* 460, 50–59

Goward, S. N., Masek, J. G., Williams, D. L., Irons, J. R., and Thompson, R. (2001). The landsat 7 mission: Terrestrial research and applications for the 21st century. *Remote Sensing of Environment* 78, 3–12

[Dataset] GVP (1994a). Report on rabaul (papua new guinea) (wunderman, r., ed.), bulletin of the global volcanism network, 19:10. smithsonian institution. `https://doi.org/10.5479/si.GVP.BGVN199408-252140`. Downloaded : 1st Feb 2021

[Dataset] GVP (1994b). Report on rabaul (papua new guinea) (wunderman, r., ed.), bulletin of the global volcanism network, 19:8. smithsonian institution. `https://doi.org/10.5479/si.GVP.BGVN199408-252140`. Downloaded : 1st Feb 2021

[Dataset] GVP (2006). Report on rabaul (papua new guinea) (wunderman, r., ed.), bulletin of the global volcanism network, 31:9. smithsonian institution. `https://doi.org/10.5479/si.GVP.BGVN200609-252140`. Downloaded : 1st Feb 2021

Hartpence, A. (2021). *Landsat Collection 2*. Tech. rep., US Geological Survey

Jutzeler, M., Marsh, R., van Sebille, E., Mittal, T., Carey, R. J., Fauria, K. E., et al. (2020). Ongoing dispersal of the 7 august 2019 pumice raft from the tonga arc in the southwestern pacific ocean. *Geophysical Research Letters* 47, e1701121

Kritten, L., Preusker, R., and Fischer, J. (2020). A new retrieval of sun-induced chlorophyll fluorescence in water from ocean colour measurements applied on olci l-1b and l-2. *Remote Sensing* 12, 3949

Melson, W. G., Jarosewich, E., and Lundquist, C. A. (1970). Volcanic eruption at metis shoal, tonga, 1967–1968: Description and petrology. *Smithsonian Contributions to the Earth Sciences* , 1–18

Miron, P., Olascoaga, M., Beron-Vera, F., Putman, N., Triñanes, J., Lumpkin, R., et al. (2020). Clustering of marine-debris-and sargassum-like drifters explained by inertial particle dynamics. *Geophysical Research Letters* 47, e2020GL089874

Pekel, J.-F., Cottam, A., Gorelick, N., and Belward, A. S. (2016). High-resolution mapping of global surface water and its long-term changes. *Nature* 540, 418–422

Qi, L., Hu, C., Mikelsons, K., Wang, M., Lance, V., Sun, S., et al. (2020). In search of floating algae and other organisms in global oceans and lakes. *Remote Sensing of Environment* 239, 111659

Roy, D. P., Wulder, M. A., Loveland, T. R., Woodcock, C. E., Allen, R. G., Anderson, M. C., et al. (2014). Landsat-8: Science and product vision for terrestrial global change research. *Remote sensing of Environment* 145, 154–172

Thomas, N., Jaupart, C., and Vergniolle, S. (1994). On the vesicularity of pumice. *Journal of Geophysical Research: Solid Earth* 99, 15633–15644

Thorpe, S. (2004). Langmuir circulation. *Annu. Rev. Fluid Mech.* 36, 55–79

Van Sebille, E., Aliani, S., Law, K. L., Maximenko, N., Alsina, J. M., Bagaev, A., et al. (2020). The physical oceanography of the transport of floating marine debris. *Environmental Research Letters* 15, 023003

Whiteside, A., Dupouy, C., Singh, A., Frouin, R., Menkes, C., and Lefèvre, J. (2021). Automatic detection of optical signatures within and around floating tonga-fiji pumice rafts using modis, viirs, and olci satellite sensors. *Remote Sensing* 13, 501

Wilson, S. T., Hawco, N. J., Armbrust, E. V., Barone, B., Björkman, K. M., Boysen, A. K., et al. (2019). Kīlauea lava fuels phytoplankton bloom in the north pacific ocean. *Science* 365, 1040–1044

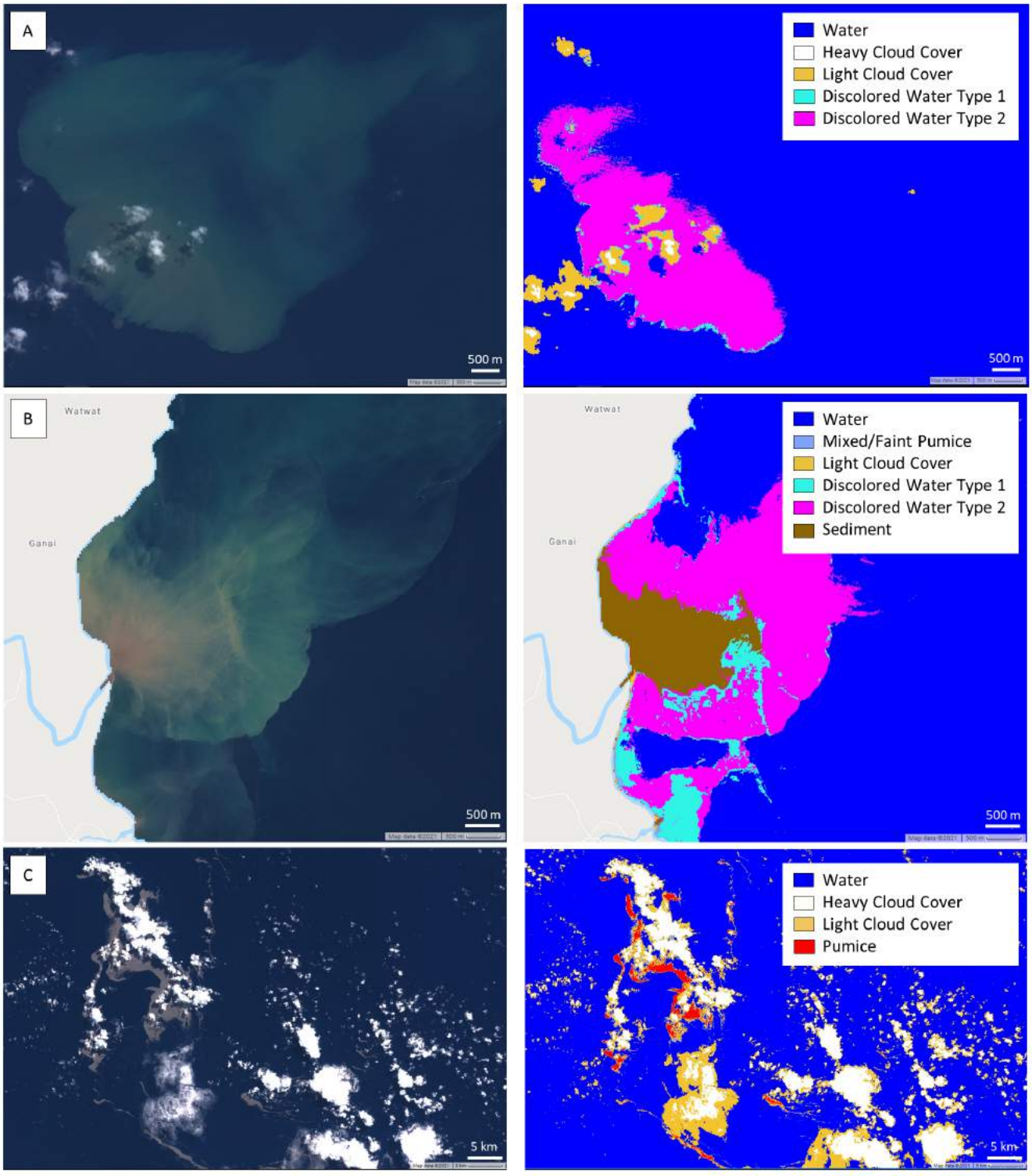

Figure S1. **(A)** RGB and classified images of Kavachi on 04/24/2020 **(B)** RGB and classified images of the river delta near Rabaul for 04/20/2020 **(C)** RGB and classified images for Tonga on 08/16/19

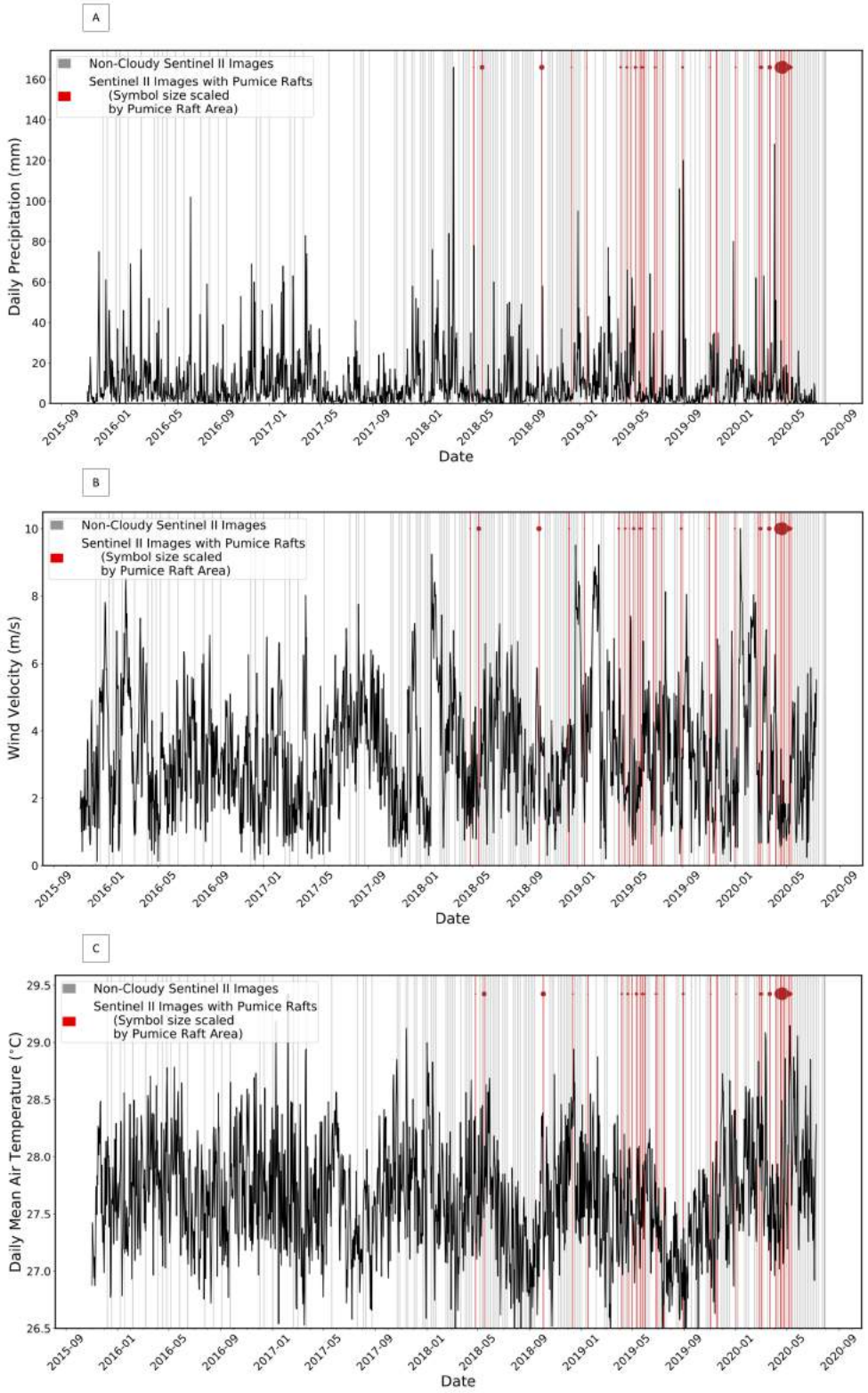

Figure S2. **(A)** Daily precipitation in Rabaul against Sentinel-2 raft detections **(B)** Daily wind velocity in Rabaul against Sentinel-2 raft detections **(C)** Daily mean air temperature in Rabaul against Sentinel-2 raft detections

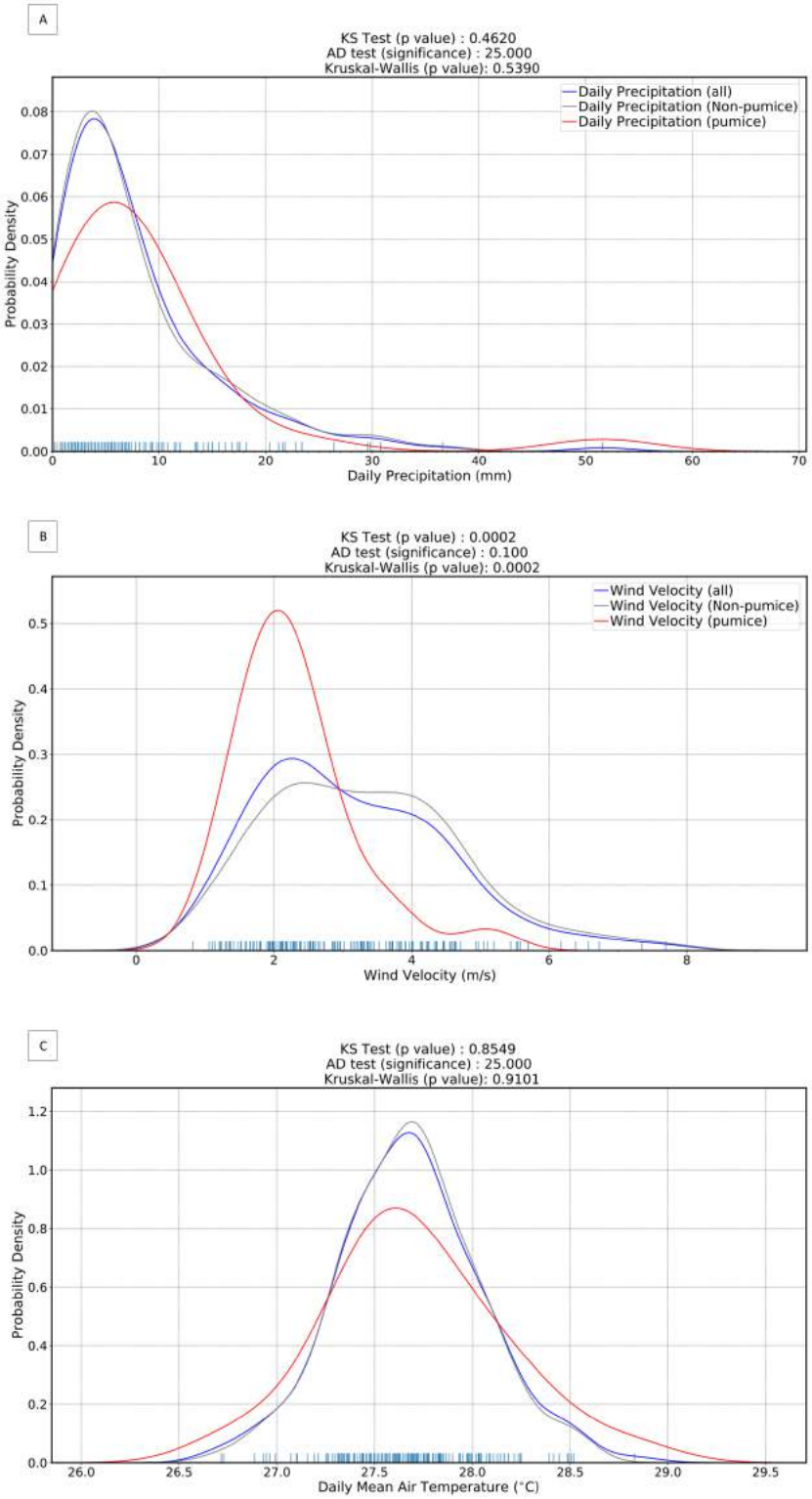

Figure S3. **(A)** Daily precipitation pdf in Rabaul (5 day rolling window) **(B)** Daily wind pdf in Rabaul (5 day rolling window) **(C)** Daily mean air temperature pdf in Rabaul (5 day rolling window)

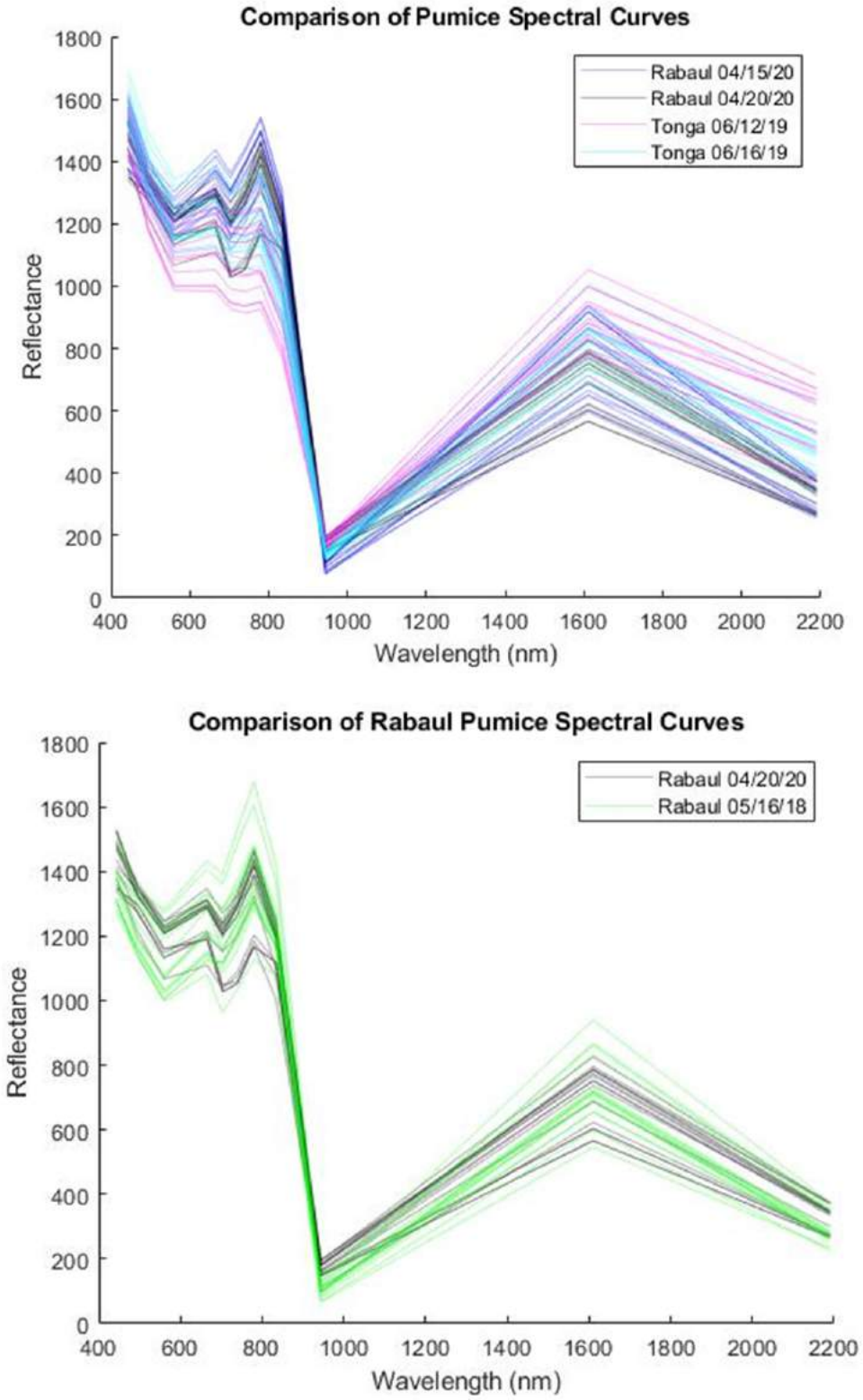

Figure S4. Comparison of pumice spectral response curves in both Rabaul and Tonga for various dates

Figure S5. Comparison of high resolution Planet Labs imagery for Tonga 2019 rafts and newly detected Rabaul rafts - These images provide examples of different raft morphologies.

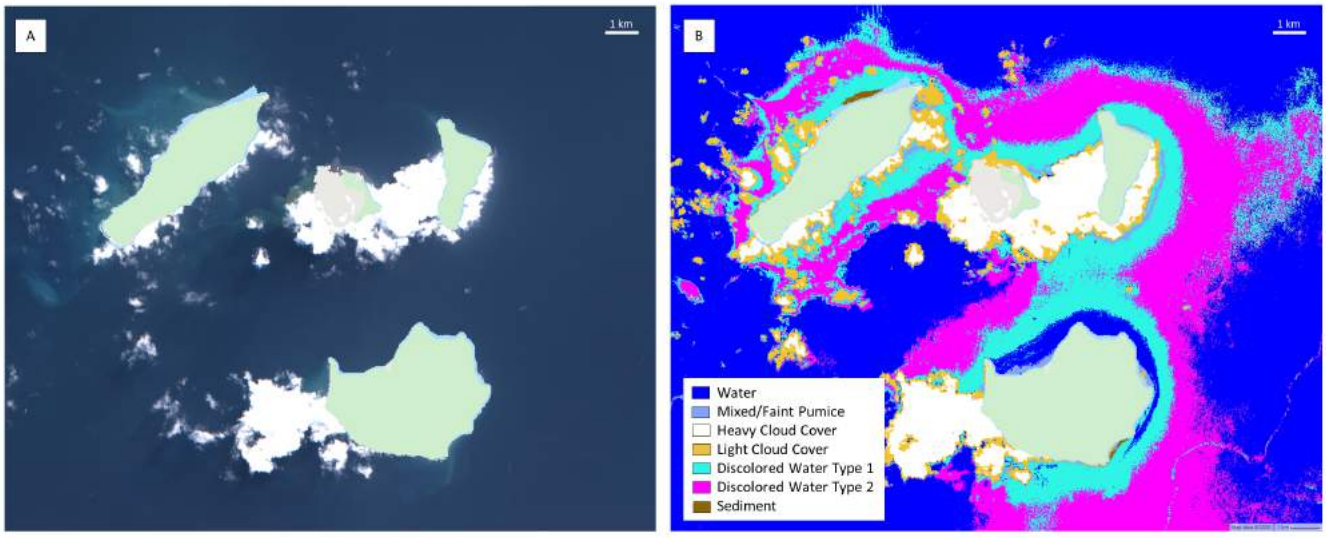

Figure S6. **(A)** RGB image of Anak Krakatau on 04/15/2019 **(B)** Classified image of Anak Krakatau on 04/15/2019

	Pumice	Water	Light Clouds	Discolored Water Type 1	Discolored Water Type 2	Sediment	Mixed Pumice	Heavy Clouds
Pumice	408	0	0	0	0	0	0	0
Water	0	1982	83	0	0	0	0	0
Light Clouds	0	0	1029	0	0	0	0	6
Discolored Water Type 1	0	0	0	0	0	0	0	0
Discolored Water Type 2	0	61	0	220	275	0	0	0
Sediment	0	0	0	0	0	78	0	0
Mixed Pumice	0	0	0	0	0	0	2	0
Heavy Clouds	0	0	0	0	0	0	0	281

Figure S7. Classification algorithm confusion matrix

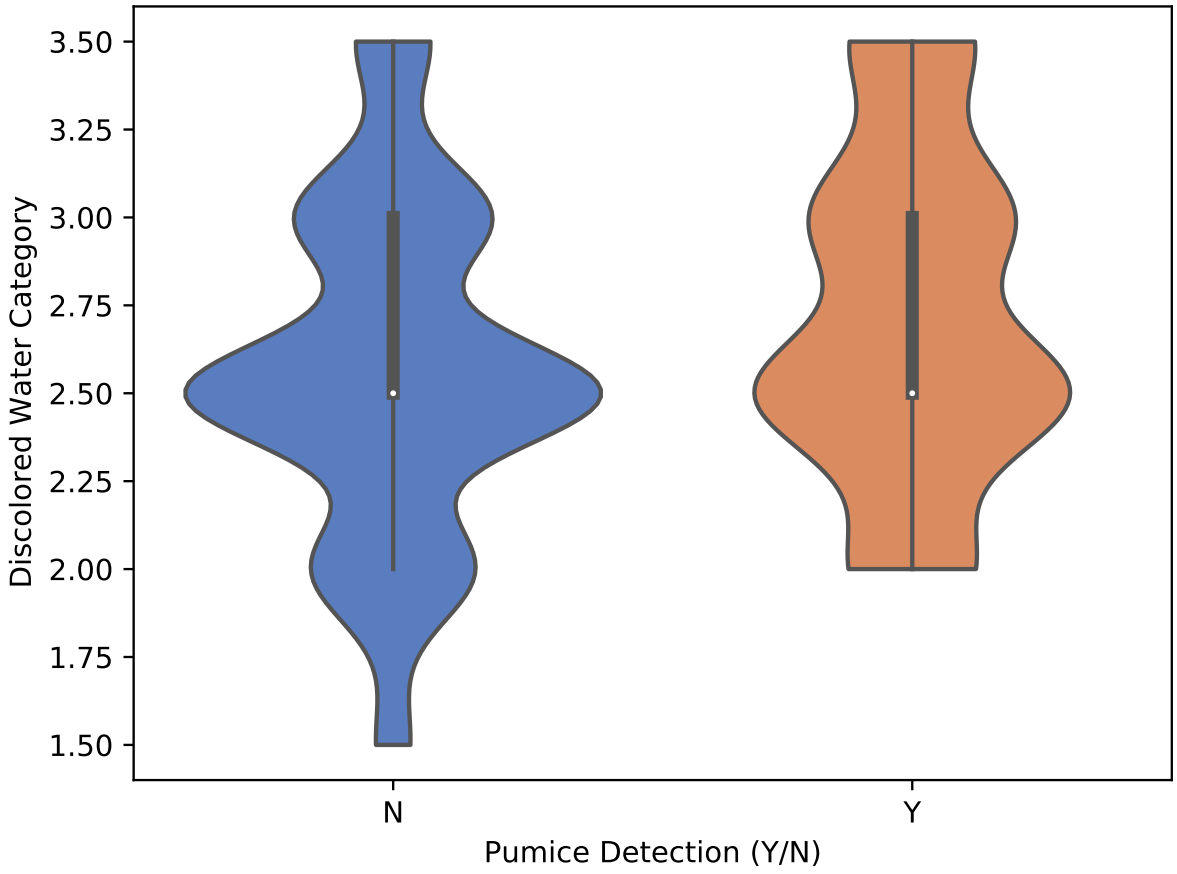

Figure S8. Comparison of pumice raft detection (Yes/No) and hydrothermal activity (discolored water category, larger values for more activity in the Tavurvur vent region) for Planet Labs detection. Note the lack of relation between the hydrothermal activity and likelihood of detecting a raft in a non-cloudy image

Figure S9. Examples of high hydrothermal activity in the Tavurvur vent region (Planet Labs Imagery) **(A)** 03/09/2011 **(B)** 09/19/16 **(C)** 01/07/18

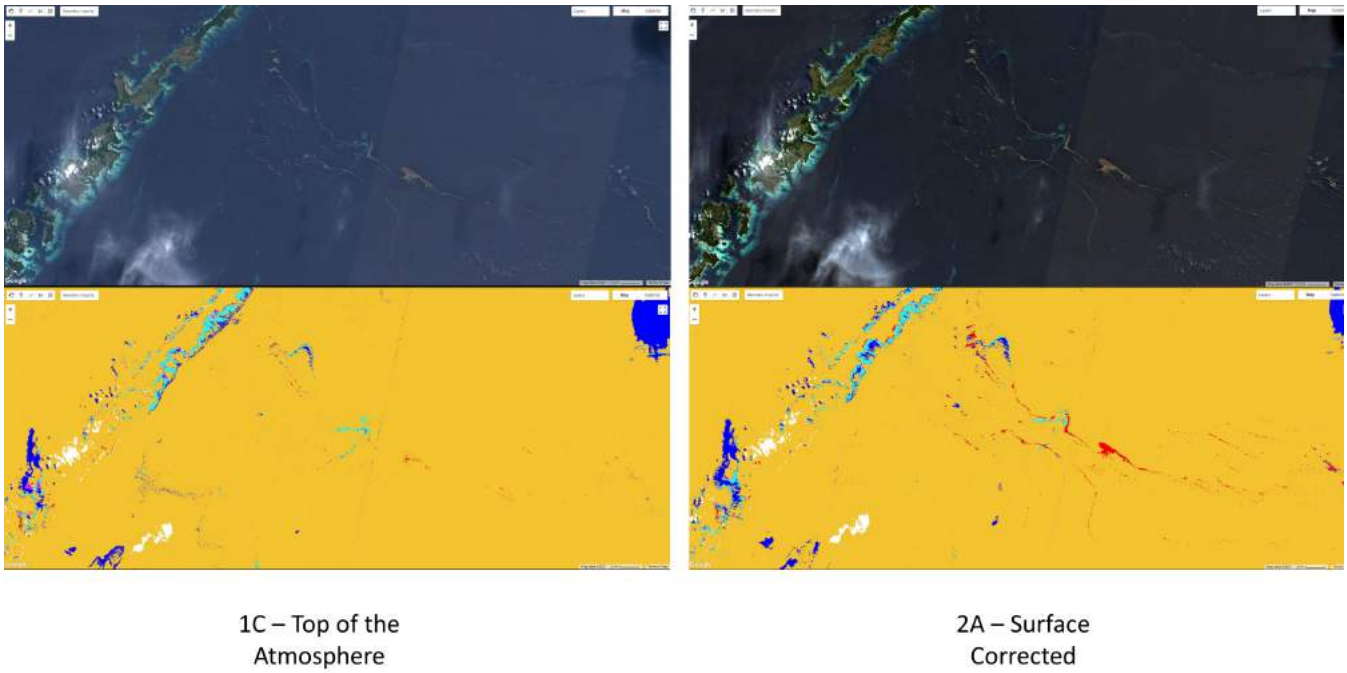

Figure S10. Comparison of using the Top-of-Atmosphere (Level-1C) vs. the atmospherically corrected Surface Reflectance (Level-2A) Sentinel-2 data products with our algorithm to detect a raft in the Tonga region on 09/29/2019

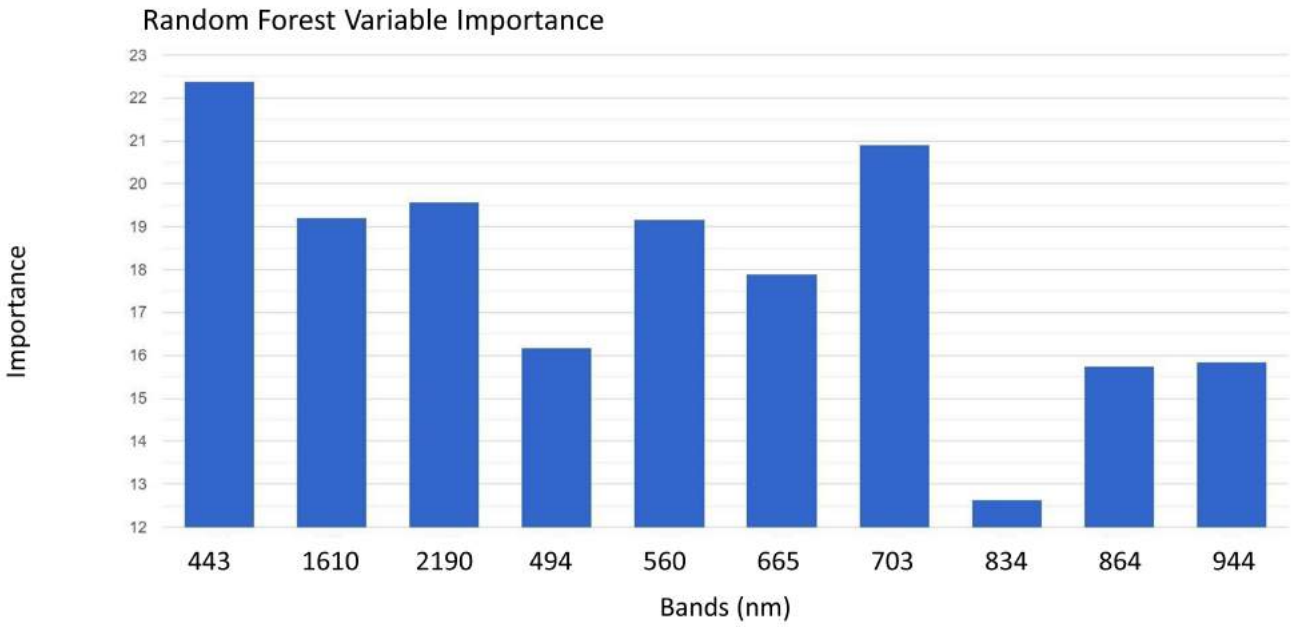

Figure S11. Importance of each Sentinel-2 band in the Random Forest algorithm. This is derived from the summed decrease in Gini impurity index for each individual over all of the trees in the RF classifier. The Gini impurity index is a measure of the probability of an observation being misclassified if it was randomly assigned to a class. The Gini index based estimate of variable importance typically provides a similar importance score for a variable's importance in classification compared to the more numerically intensive approach of permutation importance measure.